2018

PROBING TWO-DIMENSIONAL SEMICONDUCTOR AND BIOLOGICAL TISSUE BY NONLINEAR OPTICAL MICROSPECTROSCOPY

Mohammad A. Mokim
University of Rhode Island, aamtito@gmail.com

PROBING TWO-DIMENSIONAL SEMICONDUCTOR AND BIOLOGICAL TISSUE BY NONLINEAR OPTICAL MICROSPECTROSCOPY

BY

MOHAMMAD A MOKIM

A DISSERTATION SUBMITTED IN PARTIAL FULFILLMENT OF THE REQUIREMENTS FOR THE DEGREE OF

DOCTOR OF PHILOSOPHY

IN

PHYSICS

UNIVERSITY OF RHODE ISLAND

2018

DOCTOR OF PHILOSOPHY DISSERTATION

OF

MOHAMMAD A MOKIM

APPROVED:

Dissertation Committee:

Major Professor Feruz Ganikhanov

Oleg Andreev

Jason Dwyer

Nasser H. Zawia
DEAN OF THE GRADUATE SCHOOL

UNIVERSITY OF RHODE ISLAND
2018

ABSTRACT

Two-dimensional materials, such as graphene and semiconductor transition metal dichalcogenides (TMDCs), exhibit remarkable optical properties which are of great potential for applications in modern electronics. The first part of this dissertation focuses on the dispersion of the second order resonant nonlinearity ($\chi^{(2)}$) in the single layer TMDC. We begin with the study of the nonlinear optical properties of monolayer TMDC, WSe_2. We experimentally obtain the $\chi^{(2)}$ dispersion data from the single layer sample of WSe2 by using broadband ultrashort pulse laser sources. The broadband pulse is generated by specially designed photonic crystal fiber (PCF). This PCF fiber is pumped by TiS mode-locked laser to generate continuum pulse that spans from visible to near-infrared. This continuum broadband pulse is used as a fundamental beam to generate signal at the second harmonic frequency in 2D semiconductor material. We detect the signal generated in the sample by using monochrometer and charge-coupled device (CCD), which provide the spectrum of the second harmonic signal that carries the signature of the materials. To get the images of these materials, we employ an optical parametric oscillator (OPO) tuning at reasonable wavelengths. Then we shine the beam on the sample, and after the signal has been generated in the sample, it gets reflected and this beam is then collected by photomultiplier (PMT) before angle scanned using galvo-mirror scanner to provide 200x200 μm^2 imaging area. The $\chi^{(2)}$dispersion obtained with better than 3 meV photon energy resolution showed peak value being within 6.3-8.4$\times 10^{-19}$ m^2/V range. We estimate the fundamental bandgap to be at 2.2 eV. Sub-structure in the $\chi^{(2)}$

dispersion reveals a contribution to the nonlinearity due to exciton transitions with exciton binding energy estimated to be at 0.7 eV.

In the second half of this work, we study two other materials. First, we show resolution of fine spectral features within several Raman active vibrational modes in potassium titanyl phosphate (KTP) crystal. Measurements are performed using a femtosecond time-domain coherent anti-Stokes Raman scattering spectroscopy technique that is capable of delivering equivalent spectral resolution of 0.1 cm^{-1}. The Raman spectra retrieved from our measurements show several spectral components corresponding to vibrations of different symmetry with distinctly different damping rates. In particular, linewidths for unassigned optical phonon mode triplet centered at around 820 cm^{-1} are found to be 7.5±0.2 cm^{-1}, 9.1±0.3 cm^{-1}, and 11.2±0.3 cm^{-1}. Second, we demonstrate the quantitative spectroscopic characterization and imaging of biological tissue using coherent time-domain microscopy with femtosecond resolution. We identify tissue constituents and perform dephasing time (T_2) measurements of characteristic Raman active vibrations. This was shown in subcutaneous mouse fat embedded within collagen rich areas of the dermis and the muscle connective tissue. The demonstrated equivalent spectral resolution (<0.3 cm^{-1}) is an order of magnitude better compared to commonly used frequency-domain methods for characterization of biological media.

ACKNOWLEDGMENTS

I would like express my sincere gratitude to the University of Rhode Island for letting me fulfill my dream of being a student here. I would also like to thank the department of Physics for giving me the opportunity to write an honor thesis.

I would like to thank my advisor Dr. Feruz Ganikhanov for his support for making this thesis a reality. If it hadn't been for his immense support, patient and guidance, this thesis would have remained impossible. I feel privileged have Dr. Ganikhanov as my mentor.

I would like to thank my graduate program committee members Dr. Oleg Andreev, Dr. Leonard Kahn, Dr. Jason Dwyer, Dr. Michael Antosh and Dr. Dugan Hayes for giving their precious time and support.

I would like to thank all the staff members of Physics department for their support and kindness.

Thank you to all of you who had worked and have been working in our lab.

I thank my parents and my sister for always being supportive and understanding for being so far away from family.

I am grateful to my wife, Ahalam Oirdhaa, for her constant encouragement during my graduate studies and great patience at all times. I thank my two beautiful children Lamissa and Ifraz for always making me smile.

PREFACE

This dissertation is written in the 'Manuscript Format' using the Thesis/ Dissertation template of University of Rhode Island. There are three manuscripts. Figures of each manuscript are listed under the corresponding chapter in the list of figures. Detailed measurement and alignment procedure are discussed in the appendix. Essential mathematical formalisms are also provided.

The results of our studies presented here were published in three papers:

1. **M. Mokim**, A. Card, B. Sah, and F. Ganikhanov, "Dispersion of the resonant second order nonlinearity in 2D semiconductors probed by femtosecond continuum pulses." *AIP Advances* 7, 105121 (2017)

2. **M. Mokim**, CH. Carruba, and F. Ganikhanov, "Tracing molecular dephasing in biological tissues." *App. Phys. Lett.* 111,183701 (2017)

3. A. Card, **M. Mokim**, and F. Ganikhanov, "Resolving fine spectral features in lattice vibrational modes using femtosecond coherent spectroscopy." *AIP Advances* 6, 025115 (2016)

Work was presented on the following Meetings/Conferences:

1. **M. Mokim**. URI physics colloquium, RI, USA, 2018 (Talk)

2. **M. Mokim**, Feruz Ganikhanov *et al*. Optics, Laser, and Photonics, LV, USA, 2017. (Talk)

3. **M. Mokim**, Feruz Ganikhanov *et al.* APS meeting: New England section, RI, USA, 2017. (Talk)

4. **M. Mokim** *et al*. URI graduate conference, RI, USA, 2017. (Poster)

TABLE OF CONTENTS

LIST OF FIGURES

MANUSCRIPT-1

FIGURE **PAGE**

MANUSCRIPT- 1

Published in American institute of Physics (AIP) advances, October 2017

Dispersion of the resonant second order nonlinearity in 2D semiconductors probed by femtosecond continuum pulses

Mohammad Mokim, Adam Card, Bindeshwar Sah, and Feruz Ganikhanov

Department of Physics, University of Rhode Island, 2 Lippitt Road, Kingston, RI, 02881.

Corresponding Author: Feruz Ganikhanov, Ph.D.

Department of Physics

University of Rhode Island

East Hall, 2 Lippitt Road

Kingston, RI, 02881, USA

Phone: 401.874.2633

Email address: fganikhanov@uri.edu

We demonstrate an effective microspectroscopy technique by tracing the dispersion of second order nonlinear susceptibility ($\chi^{(2)}$) in a monolayer tungsten diselenide (WSe_2). The $\chi^{(2)}$dispersion obtained with better than 3 meV photon energy resolution showed peak value being within 6.3-8.4×10^{-19} m^2/V range. We estimate the fundamental bandgap to be at 2.2 eV. Sub-structure in the $\chi^{(2)}$dispersion reveals a contribution to the nonlinearity due to exciton transitions with exciton binding energy estimated to be at 0.7 eV.

Two-dimensional materials have attracted very strong interest due to their promise in practical applications. For example, monolayer MoS_2 has been shown recently as an efficient material for low-power field effect transistors [1]. Strongly enhanced second order optical nonlinearity $\chi^{(2)}$ in monolayers of transition metal dichalcogenides (TMDC) is also predicted due to the lack of an inversion center in their crystalline structure. The reported absolute values of $\chi^{(2)}$ vary though by orders of magnitude 5 -10^5 pm/V [2-4]. Very few studies though address the spectral response of $\chi^{(2)}$. This type of data can provide new information along with the results of traditional optical methods for condensed matter characterization. Wang et al. [5] performed experiments on obtaining $\chi^{(2)}$dispersion in WSe_2 at low temperatures. Multiple peaks in $\chi^{(2)}$ dispersion within SHG photon energy range of 1.7-2.4 eV were clearly attributed to excitons with n=1-3. Large variations in the SHG signal have made this point-by-point measurement insensitive to smaller features in the SHG spectra. In addition, the incident photon energy range was limited so that the near bandgap nonlinear optical response of the material could not be obtained.

In this letter, we report on a microspectroscopy method applied to characterize monolayer WSe_2 within a photon energy range of 2.4-3.2 eV. We detect single-shot second harmonic (SH) spectra from monolayer WSe_2 material with better than 0.3 nm resolution (~3 meV) and low noise (5-6% rms) using broadband femtosecond continuum pulses. Fine sub-structure features that can be detected within the main peak of $\chi^{(2)}$ indicate the impact of near bandgap exciton transitions. We retrieve, with a fairly good precision, the fundamental bandgap and exciton binding energy. The absolute values for $\chi^{(2)}$ are also provided. We believe that our experimental results will aide in developing refined theoretical models for 2D materials.

The experimental idea is presented in Fig. 1(a). Femtosecond continuum pulses with a smooth spectral envelope centered in the near-IR are used to generate SHG signal within an atomically thin semiconductor sample. Spectrum of the second harmonic signal that carries spectral signatures of the sample is then detected with fine (~3 meV) spectral resolution. Laser part of the experimental arrangement, shown in Fig. 1(b), generates spectrally smooth shape for the ultra-broad continuum in the near infrared (780-1050 nm) with typical power density of ~50 μW/nm. Chromatic dispersion compensated optics were used to deliver the fundamental beam to the sample within less than 400 nm spotsize. The incident beam can be angle scanned using galvo-mirror scanner to provide 200×200 μm^2 imaging area. SH signal from the sample was collected through the same objective lens in the backward direction. The SHG signal spectra were resolved using monochromator (Horiba, Inc. model: iHR320) and cooled CCD detector (Syncerity-UV/Vis, Horiba Inc.) Single layer WSe_2 flakes were prepared by micromechanical cleavage of bulk WSe_2 crystal on 90 nm SiO_2 on a

Si substrate. Figure 2(a) shows SHG image of the flake. We present SEM image of the flake in Fig. 2(b). The flake also characterized in a separate photoluminescence measurement. The latter reveals a narrow (~45 meV) peak at 746 nm (~1.662 eV) that is shown in Fig. 2(b) and corresponds to the first exciton line characteristic for single layer. We have checked the SHG signal dependency versus incident power of the fundamental beam to reveal the quadratic increase shown in Fig. 2(d). The SHG image shown in Fig. 2(a) displays high contrast and absence on any appreciable signal from interfaces other than the one created by the flake. Fairly large SHG signal variations (up to 30%) are observed even within the unripped parts of the flake (Fig 2(e)). We believe that this is due to local field variations affecting $\chi^{(2)}$ at the flake/SiO_2 interface. The SHG spectrum is shown in Fig. 3(a) by the blue curve. We have also performed, for comparison purposes, point-by-point wavelength tuning SHG measurements with wavelength tunable Ti:sapphire oscillator (filled circles data in Fig 3(a)). The SHG signal fluctuations are significantly higher ($\sigma=\pm 54\%$) for this case. We believe that much higher SHG signal variations versus wavelength observed in the point-by-point measurements are couple of additional sources of the variation. Namely , changes in the fundamental field parameters like pulsewidth and spatial mode while the wavelength is tuned. The lowered precision for the SHG spectra were also observed in the referred point-by-point measurements [5] as authors pointed to the uncertainties in the pulsewidths while the wavelength was tuned as being the main reason.

The observed increase in the resonant nonlinearity $\chi_{2D}^{(2)}$ matches well with split-off band transitions (i.e. B-exciton) if one considers bandstructure parameters for

single layer of WSe_2 at K-point such as bandgap (E_g) and split-off energy (Δ_{SO}) [5, 6]. A similar effect has been observed in MoS_2 involving a different energy valley that is at Γ point [3].

We have obtained $\chi_{2D}^{(2)}$ spectra two approaches. The first one exploits the relationship between the fundamental and SH powers. In the other one we used comparative approach when a material with known second order nonlinearity is used. We have chosen thin KTP crystal. The crystal is well characterized from many aspects. The second order effective nonlinearity (d_{eff}) is between 1.72-2.01 pm/V [7] for the incoming beam polarization and crystal orientation that we used. By normalizing our WSe_2 SH data to the one obtained from the crystal (P_2^B), we obtain a ratio ($\rho = P_2^{2D}/P_2^B$) that provides dispersion of the absolute value of $\chi_{2D}^{(2)}$ and is free from measurement artifacts (e.g., $T_{2\omega}$, etc.). The result is displayed in Fig. 3(b) by blue curve for a comparison. Some difference can be seen at lower photon energies. We note that SHG and fundamental signal have been detected by different spectral devices in the first method. The second method is free from artifact.

Bloembergen et al [8] were first to consider SHG from thin layers and interfaces. SHG power has been derived by Merano [9] by considering real experimental situation of a sheet of 2D material on the top of the layered substrate. Following the approach developed in [9,10] and making use of the results by Boyd et al. [11] SHG pulse peak power from 2D material (P_2^{2D}) and bulk crystal (P_2^B) can be expressed as shown in Supplement [12]. Based on that, the absolute value of $\chi_{2D}^{(2)}$ expressed in

terms the crystal's effective nonlinearity d_{eff}, refractive index (n_b), numerical aperture of the objective lens (Θ) and the measured ratio (ρ) is:

$$\chi_{2D}^{(2)} = \frac{16\lambda_1\sqrt{\rho}}{\left|(1+r_\omega)^2(1+r_{2\omega})\right|(n_b+1)^3\sqrt{n_b}\Theta^2}\left|d_{eff}\right| \quad (1)$$

It is important to note that the two-layered substrate can lead to the enhancement or attenuation of the SHG intensity due to interference effects that depends on the thickness of the SiO_2 layer. This is taken into account in the factor containing complex field reflectivity ($r_\omega, r_{2\omega}$). With the help of formula (1), we can provide absolute scaling for the result shown in Fig. 3(b) (left scale). For KTP material the refractive index (n_b) changes by only few percent within the photon energy range that we have. The median peak value of $\chi_{2D}^{(2)}$ for WSe_2 monolayer at the SH photon energy of 2.76 eV can be estimated at 7.3×10^{-19} pm^2/V. We provide ±15% range owing to several factors such as the range for d_{eff} itself and taking into account signal variations across the flake that were discussed earlier. The value is on the same order of magnitude with the one quoted for the measured MoS_2 sheet nonlinearity in [13] and factor of 2.7 smaller than the one provided by Merano [9] for MoS_2. If we straightforwardly use solutions provided in [8] and assume that the sample still has bulk refractive index [14] and nonlinearity $\chi_{2D}^{(2)}$ (in units of m/V) the expression for estimate is:

$$\left|\chi_{2D}^{(2)}\right| = \sqrt{\rho}\,\frac{8\pi\sqrt{f(n')}}{\sqrt{n}(n+1)^3\Theta^2|\zeta|}\left|\chi_B^{(2)}\right| \quad (2)$$

In the formula above, $f(n')$ is a factor containing refractive indices of bulk WSe_2 and is coming from solutions for the SH field [17], ζ -factor accounts for the interference

effects. Additional details are provided in Supplement [12]. This approach may cause controversy and disagreement. We, however, we would like to provide an estimate just for sake of comparing the material's nonlinearity with the one of other bulk non-centrosymmetric semiconductors. The estimated $\chi_{2D}^{(2)}$ value is in the 932-1233 pm/V range for peak SH photon energy while the off-peak value is about 440 pm/V.The values are comparable with the ones for well known non-centrosymmetric semiconductors (GaAs, CdTe, ZnSe [15]) that are used in parametric devices and frequency converters in the infrared [16]. Comprehensive theoretical treatment and modeling of the second order nonlinearity is based on rigorous approaches outlined in [17,18]. Here we will use an approach based on parabolic bands approximation, accounting for Coulomb effects via exciton continuum states above bandgap in order to estimate dispersion of the absolute value of $\chi^{(2)}$ due to interband transitions first. The expression for $\chi^{(2)}$ along the electric field and induced dipole moment in *x*-direction can be represented by [18]:

$$\chi_{XXX}^{(2)}(2\omega) = -\frac{ie^3}{2m^3\omega^3}\sum_{\vec{k}}\sum_{vcc'} M_{vc}^{X} M_{cc'}^{X} M_{c'v}^{X} F_{v,c,c'}(\omega) \tag{3}$$

$$\begin{aligned} F_{cc'k}(\omega) &= D_{cc'k}(\omega,2\omega) + D_{cc'k}(\omega,-\omega) + D_{cc'k}(-\omega,-2\omega) \\ D_{v,c,c'}(\omega,2\omega) &= \frac{1}{\left(E_{cv}(\vec{k}) - i\gamma_{cv}(\vec{k}) - 2\hbar\omega\right)\left(E_{c'v}(\vec{k}) - i\gamma_{c'v}(\vec{k}) - \hbar\omega\right)} \end{aligned} \tag{4}$$

M_{vc}^{X} - factors represent momentum matrix elements for valence to conduction, conduction to upper conduction band transitions, $E_{cv}(\vec{k})$ is energy difference between bands, $\gamma_{cv}(\vec{k})$ is the interband polarization dephasing rate. We have considered four parabolic energy bands near *K*-point of the Brillouin zone (*BZ*). Those include two

valence bands with split off energy difference of $\Delta_{SO} = 0.52eV$, with the effective masses of $m_v = 0.52m_e, m_{so} = 0.51m_e$ and two conduction bands with the effective masses of $m_c = 0.53m_e, m_{c'} = 0.92m_e$ and energy difference at K-point $\Delta_{cc'} = 1.79eV$ [6]. We have also considered momentum matrix elements and dephasing rates are *k*-, and therefore energy, independent. The summation over *k*-states can be replaced by integral over energy that couples the resonant denominator in formula (4) and joint density of states factor for the first conduction and top valence bands for continuum excitons $\left(\sigma(E_{cv}) \approx \left(1 - \exp\left(-\left(13.6eV\, m_R/m_e\left(E_{cv} - E_g\right)\right)^{1/2}\right)\right); E_{cv} \rangle E_g\right)$. Figure 4 shows the results of our calculations when γ was set to 35 meV. It is important to note that the nonlinearity is sensitive to a change of E_g. This is shown by comparing two simulations when E_g is changed from 2.22 eV (green curve) to 2.15 eV (dash-dotted curve). It is apparent that when the bandgap is set at ~ 2.2 eV a better match with the experimental data around the peak area is obtained. We believe that band non-parabolicity becomes critical to explain the experimental data at higher photon energies. On the lower energy side one finds that the rise in simulated $\chi^{(2)}$ is noticeably sharper when compared to our experimental data. The discrete exciton contributions can be represented mainly by resonant factors that are similar to the term in formula (4) with peak energies $E_n = E_0/(n-1/2)^2$ used instead of $E(k)$. There are at least two clearly pronounced peaks in the experimental curve at photon energies of 2.64 eV and 2.69 eV. The 50 meV energy difference matches well for *n*=2 and *n*=3 excitons when the binding energy $4E_0 = 0.71eV$ is assumed. Figure 4(b) shows total nonlinearity due to the interband transitions and multiple exciton lines (*n=1-5*) below

the first conduction band states. The best fit is obtained for the exciton binding energy of 0.71 eV while the bandgap (E_g) parameter was set at 2.22 eV. The obtained value for the bandgap matches well with the ones reported in [5,6]. Exciton binding energy obtained from our data is also in close agreement with the value of 0.6±0.2 eV reported by Wang et al. [5].

In conclusion, we have demonstrated precise measurements of the second order nonlinearity in atomically thin layer of semiconducting material within broad range of photon energies. Using ultra-broadband continuum pulses, we were able to detect fine features in the $\chi^{(2)}$ dispersion with high spectral resolution (<3 meV). The nonlinearity onset is primarily due to monolayer WSe_2 states that couple valence bands, excitonic levels and the continuum states above the first conduction band. Using our data, we estimate peak nonlinearity range for a sheet of WSe_2 at 6.3-8.4×10^{-19} m^2/V and 932-1233 pm/V if we assume the existence of bulk properties. We also obtained from our data the room temperature bandgap and exciton binding energy that are estimated at 2.2 eV and 0.7 eV correspondingly. Our results show that the experimental $\chi^{(2)}$ dispersion data provide clear resolution of the near band-gap exciton states in comparison with traditional linear methods that target measurement of the linear dielectric function.

Funding

National Science Foundation (NSF) (DBI-1355307) and University of Rhode Island start-up funds.

References

[1]B. Radisavljevic, A. Radenovic, J. Brivio, V. Giacometti, and A. Kis, "Single-layer MoS_2 Transistors," Nat. Nanotechnol. **6**, 147-150 (2011).

[2]N. Kumar, S. Najmaei, Q. Cui, F. Ceballos, P. M. Ajayan, J. Lou, and H. Zhao, "Second harmonic microscopy of monolayer MoS_2," Phys. Rev. B **87**, 161403-5 (2013).

[3]L. M. Malard, T. V. Alencar, A.P.M. Barboza, K. F. Mak, and A.M. de Paula, "Observation of intense second harmonic generation from MoS_2 atomic crystals," Phys. Rev. B **87**, 201401-5 (2013).

[4]E. Mishina, N. Sherstyuk, S. Lavrov, A. Sigov, A. Mitioglu,S. Anghel, and L. Kulyuk, "Observation of two polytypes of MoS_2 ultrathin layers studied by second harmonic generation microscopy and photoluminescence," Appl. Phys. Lett. **106**, 31901-5 (2015).

[5]G. Wang, X. Marie, I. Gerber, T. Amand, D. Lagarde, L. Bouet, M. Vidal, A. Balocchi, and B. Urbaszek, "Giant Enhancement of the Optical Second-Harmonic Emission of WSe_2 Monolayers by Laser Excitation at Exciton Resonances,"Phys. Rev. Lett. **114**, 097403-6 (2015).

[6]A. Ramasubramaniam, "Large excitonic effects in monolayers of molybdenum and tungsten dichalcogenides," Phys. Rev. B **86**, 115409-6 (2012).

[7]V. G. Dmitriev, G. G. Gurzadyan, *Handbook of Nonlinear Optical Crystals* (Springer Series in Optical Sciences), 2d Edition, (1996).

[8]N. Bloembergen, P.S. Pershan , "Light Waves at the Boundary of Nonlinear Media ," Phys. Rev. **128**, 606-622 (1962).

[9]M. Merano, “Nonlinear Optical Response of a Two-dimensional atomic crystal,” Opt. Lett. **41**,187-190 (2016).

[10]M. Merano, “Fresnel coefficients of a two-dimensional atomic crystal,” Phy. Rev. A **93**, 013832 (2016)

[11]G.D. Boyd, D.A.Kleinman, “Parametric interaction of Focused gaussinan light beams ,” J. Appl. Phys. **39**, 3597-3639 (1968).

[12]Supplement

[13]Y.Li, Y.Rao, K.F.Mak, Y.You, S.Wang, C.R.Dean, and T.F.Heinz,“ Probing symmetry properties of Few-layer MoS_2 and h-BN by optical second-harmonic generation,” Nano Lett. **13**, 3329-3333 (2013).

[14]S.M. Eichfeld, C.M.Eichfeld, Y-C. Lin, L. Hossain. J.A.Robinson, “Rapid, non-destructive evaluation of ultrathin WSe2 using spectroscopic ellipsometry,” APL Mater. **2**, 092508 (2014).

[15]I. Shoji, T. Kondo, A. Kitamoto, M. Shirane, and R. Ito, “Absolute scale of second-order nonlinear-optical coefficients,”J. Opt. Soc. Am. **14**, 2268-2294 (1997)

[16]K. Vodopyanov, O. Levi, P.Kuo, T. Pinguet, J.Harris, M.Fejer, B. Gerard, L. Becouarn, and E. Lallier, “Optical parametric oscillation in quasi-phase-matched GaAs” Opt. Lett. **29**, 1912-1914 (2004) .

[17]M. L. Trolle, G. Seifert, T. G. Pedersen ,"Theory of excitonic second harmonic generation in monolyaer MoS_2," Phys. Rev B **89**, 235410 (2014).

[18]R. Leitsmann, W.G.Schmidt, P.H.Hahn, and F.Bechstedt, “Second-harmonic polarizability including electron-hole attraction from band-structure theory,” Phys. Rev. B **71**, 195209 (2005).

Figure 1.

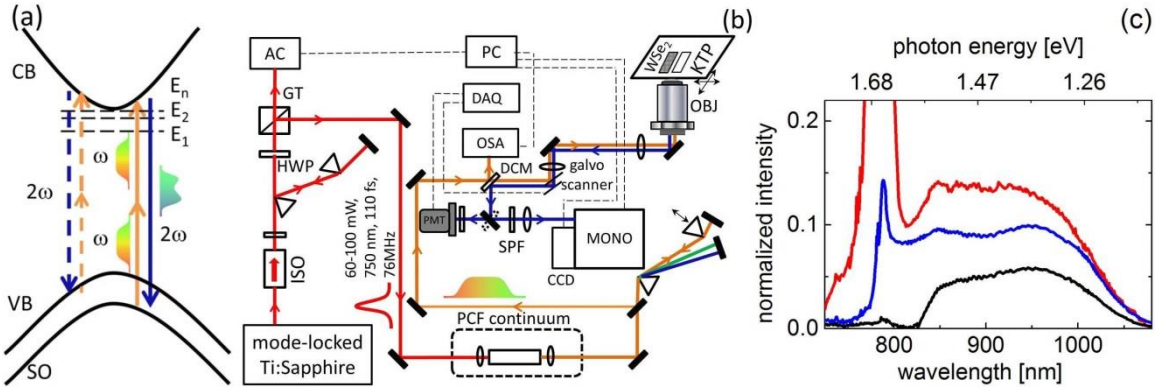

Fig. 1. (a) Photon diagram SHG process in monolayer semiconductor. (b) Setup: ISO- optical isolator, PCF –photonic crystal fiber, DCM- dichroic mirror, OBJ-high numerical aperture objective lens, SPF-short pass filter. Broadband near-IR pulse derived from femtosecond continuum serves as fundamental beam. Spectra of the generated second harmonic pulses carrying resonant features are analyzed. (c) spectra of the femtosecond continuum, used as a fundamental beam, obtained by moving the second dispersive prism in the set up (see part (b)) into the beam with the spectrum shown in red corresponding to more prism insertion.

Figure 2.

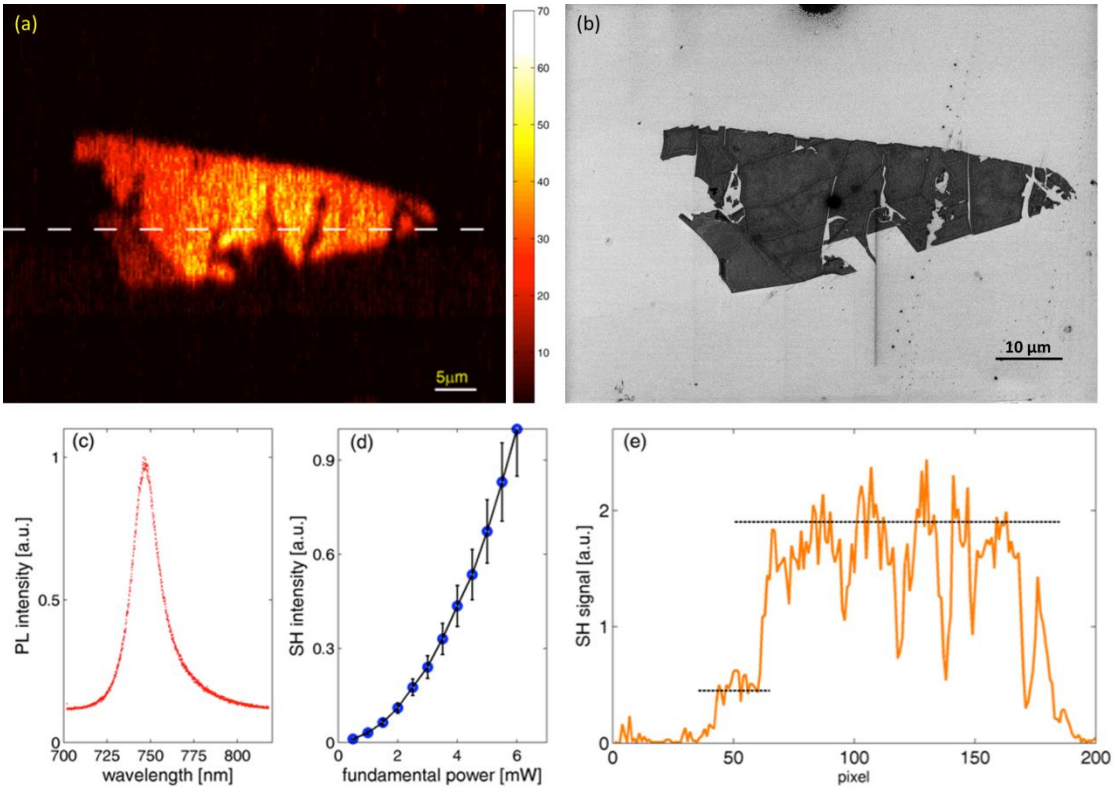

Fig. 2. (a) SHG image of a single layer WSe_2 flake. Lower left corner of the sample contains three WSe_2 layers and therefore show four times smaller signal. (b) SEM image of the same area with about 10 nm spatial resolution (c) Photoluminescence data obtained from the flake when it was excited by 532 nm continuous wave beam, (c) detected second harmonic beam power versus power of the fundamental beam, (d) SHG signal change across the image along the dashed line.

Figure 3.

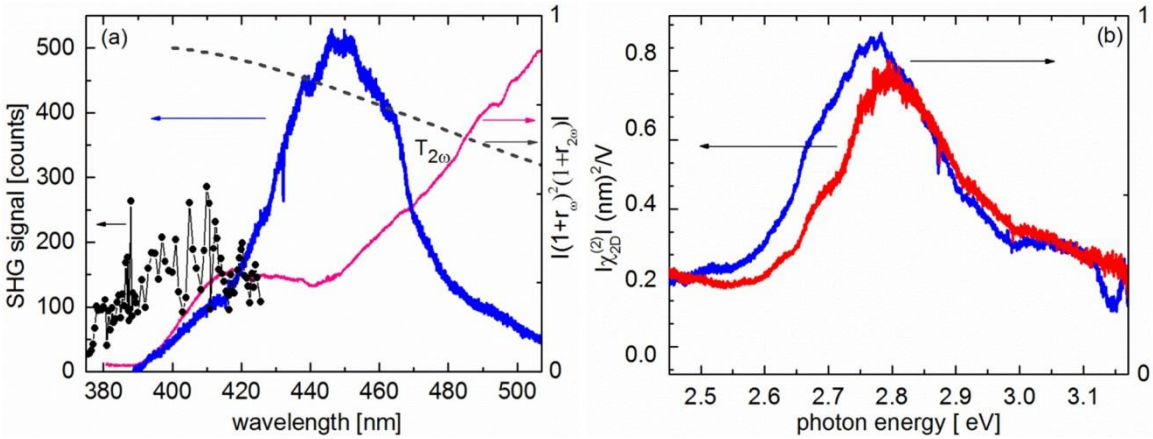

Fig. 3. (a) Second harmonic signal spectrum (P_2^{2D}) detected from monolayer part of WSe_2 sample (blue), relative transmission (T_ω) of the optical system versus wavelength (cyan), calculated enhancement factor ζ (black dash); (b) resulting absolute value of the second order nonlinearity ($\chi^{(2)}$) obtained by power relationship (blue curve) and the comparative method using KTP crystal (red curve).

Figure 4.

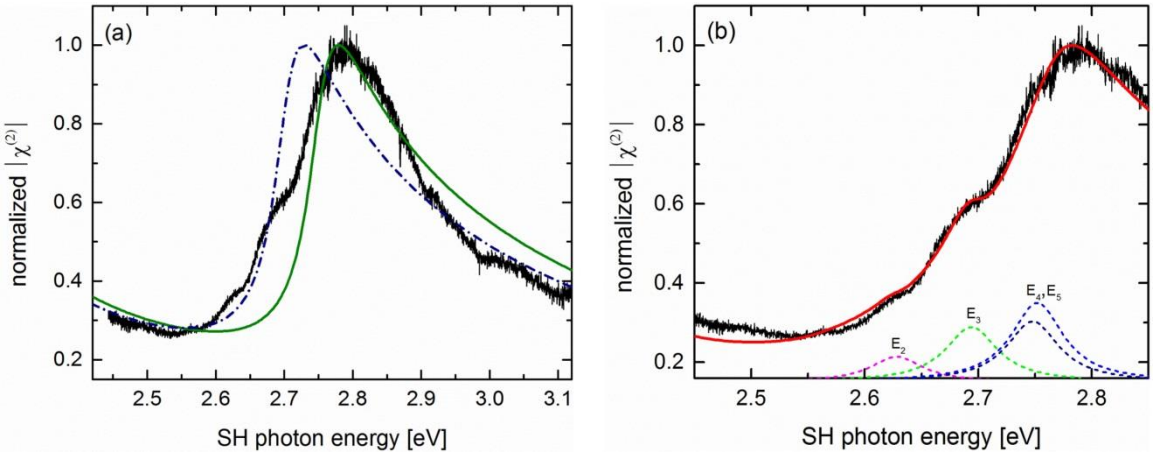

Fig. 4. (a) Normalized $\chi_{2D}^{(2)}$ versus SH photon energy (black curve). Green solid curve is the result of $\chi_{2D}^{(2)}$ calculations for E_g =2.21eV while changing the parameter to 2.15eV results in the blue dash-dotted curve. (b) Experimental $\chi_{2D}^{(2)}$ dispersion (black line) and result of calculations accounting for contributions due to exciton states with energies E_n below the bandgap. Colored (dashed) lines show contributions to the nonlinearity from broadened ($\Delta\nu_n = 35-42meV$) exciton lines with the main quantum numbers n=2-5.

MANUSCRIPT- 2

Published in American institute of Physics (AIP) advances, February 2016

Resolving fine spectral features in lattice vibrational modes using femtosecond coherent spectroscopy

Adam Card, Mohammad Mokim, and Feruz Ganikhanov

Department of Physics, University of Rhode Island, 2 Lippitt Road, Kingston, RI, 02881.

Corresponding Author: Feruz Ganikhanov, Ph.D.

Department of Physics

University of Rhode Island

East Hall, 2 Lippitt Road

Kingston, RI, 02881, USA

Phone: 401.874.2633

Email address: fganikhanov@uri.edu

We show resolution of fine spectral features within several Raman active vibrational modes in potassium titanyl phosphate (KTP) crystal. Measurements are performed using a femtosecond time-domain coherent anti-Stokes Raman scattering spectroscopy technique that is capable of delivering equivalent spectral resolution of 0.1 cm^{-1}. The Raman spectra retrieved from our measurements show several spectral components corresponding to vibrations of different symmetry with distinctly different damping rates. In particular, linewidths for unassigned optical phonon mode triplet centered at around 820 cm^{-1} are found to be 7.5±0.2 cm^{-1}, 9.1±0.3 cm^{-1}, and 11.2±0.3 cm^{-1}. Results of our experiments will ultimately help to design an all-solid-state source for sub-optical-wavelength waveform generation that is based on stimulated Raman scattering.

Precise information on fine structure and decay of Raman active modes is essential from both fundamental and device applications point of views. Time-domain studies provide direct information on decay and dephasing processes for vibrational modes and, for solid-state media, provide most valuable information as concerned parametric phonon interaction due to deformation potential anharmonicity. In frequency domain, dispersion of the corresponding nonlinear optical susceptibility is an essential charcateristic in order to get an insight into physics of intra- and interatomic groups interactions. In this paper we focus on an important nonlinear optical gain material that is used both as intracavity and external gain material in multi-wavelength laser devices. The attention has recently grown due to possible applications of efficient frequency converters in generating phase-locked frequency combs for attosecond waveform generation. Potassium titanyl orthophosphate

$KTiOPO_4$ (KTP) is a widely known optical material that is particularly attractive for nonlinear optical applications. Because of its high nonlinear optical coefficient and its optical and mechanical stability, the crystal is used in laser sources as an optical frequency converter. Its large electro-optic coefficient, low dielectric constant and ion exchange properties also make it suitable for electro-optic [1] and waveguided laser devices [2]. The crystal was previously shown to be an efficient source for multi-wavelength pulse generation via stimulated Raman scattering (SRS) [3,4] or as a combination of SRS and efficient second order frequency conversion [5]. Renewed interest came with recent SRS experiments on high-frequency crystal vibrations that promised a pathway towards a solid-state sub-optical-cycle waveform source [6-8]. In other words, materials with high second and third order nonlinearity associated with several Raman active vibrations at high frequency range are of interest from the standpoint of generating a frequency comb that would ultimately support attosecond waveforms [9]. Knowledge of key properties of lattice vibrations is thus important in the light of the applications of this material as a nonlinear gain (of both second and third order) medium.

KTP's vibrational spectra are quite complex. The spectra consist of about 100 Raman active peaks as a result of the crystal's multiatomic unit cell. The complexity makes it difficult to perform comprehensive and unambiguous phonon line assignment, to precisely measure bandwidth and separation of individual Raman active peaks, as well as to estimate Raman cross-section for each individual phonon line. Even though the material has been known for more than three decades, detailed spectroscopic studies on its Raman active vibrations are relatively scarce [10-12]. The

performed studies helped to elucidate contributions to Raman and infrared spectra from major atomic units within the primitive cell, as represented by TiO_6 octahedra and PO_4 tethrahedra. Also, important details concerning line assignments and their major characteristics were provided by the studies. However, the information ultimately proved to be contradictory and detailed spectral features of some peaks were not provided by these experiments. In particular, the first comprehensive Raman study of KTP [10] assigned peaks at around 818 cm^{-1} to the ν_1 symmetric stretching mode within slightly distorted PO_4 tetrahedra simply due to the fact that the line does not show up in the infrared reflectivity spectra. There are either two or three components spaced apart by approximately 16-40 cm^{-1} with linewidths within the 15-25 cm^{-1} range, depending on the vibrational mode symmetry. Another study characterized Raman peaks in the vicinity of 800 cm^{-1} as most likely belonging to TiO_6 octahedra vibrational modes of different symmetry, providing mode separations within 11-38 cm^{-1} and the linewidth range of 9.2-16.4 cm^{-1} [11]. A study that followed later stated that the Raman line detected at ~830 cm^{-1} is an intergroup (Ti-O-P) vibration, but provided no details on the detected linewidths and separations for the different peaks [12].

At room temperature, the Raman spectroscopy of KTP has also been investigated from 10 to 1400 cm^{-1} [13-14] and also studied as a function of high pressure revealing the existence of two additional phase transitions near the critical pressures of 5.5 and 10 GPa [15]. Temperature dependent Raman scattering were studied [16-17] and found that no phonon mode coalesces to central peak near T_c and reported it as a sign of damped soft mode [16]. A study on polarized Raman spectra showed strongest phonon

line located at 234 cm^{-1} [18]. It is worth mentioning that no experimental or theoretical study can be found which addresses phonon dispersion properties or mechanisms for phonon line decay. As was mentioned above, there is a motivation for a more detailed characterization of phonon vibrations in the material in the light of a search for an efficient solid-state media for a sub-optical-waveform source. Indeed, the crystal possesses several high-scattering cross-section phonon modes within energy range of 200-1000 cm^{-1}. The modes are conveniently spaced apart so that generation of a frequency comb, via SRS with intrinsically phase-locked spectral components, would provide multi-octave bandwidth to support sub-femtosecond pulses.

In this work, we present data on the decay of some of the KTP crystal phonon modes within 640-850 cm^{-1}. We reveal the fine structure of the vibrations by retrieving the vibrational system's response function and Raman spectra. Our data provide details on the crystal's complex vibrational spectra supported by important quantitative results. The data obtained for an unassigned vibrational mode at 820 cm^{-1} supports the conclusion that the modes decay noticeably slower when compared to high-frequency modes originating from vibrations of the main TiO_6 or PO_4 atomic groups. We attempt to explain our linewidth results within the framework of parametric phonon interaction due to the deformation potential anharmonicity.

Time-domain CARS spectroscopy is a valuable tool that enables probing the dynamics of elementary excitations in condensed matter. This technique monitors in time a degree of coherence within the lattice or molecular vibrations created by two ultrashort optical pulses at an earlier moment of time. Tracing the net coherence provides information on characteristic relaxation and dephasing processes. In our

studies we employed three-color CARS geometry with widely tunable 110-150 fs pulses [19,20]. The experimental set up is schematically shown in Figure 1. The two pulses that are needed to coherently drive lattice vibrations within a sample's macroscopic volume are provided by synchronously pumped optical parametric oscillators (OPOs) running at 76 MHz. The OPOs utilize high parametric gain periodically poled lithium tantalate (PPSLT) crystals. The OPOs were simultaneously pumped by a split output of a high-power mode-locked Ti:sapphire oscillator tuned to 765 nm. Detailed OPO characteristics and performance were reported in our recent publications [21,22]. The OPOs with pulsed outputs at 970-1020 nm and 1050-1100 nm, served to coherently drive lattice vibrations with energies within 600-990 cm^{-1}. Another small part of the Ti:sapphire oscillator was delayed and served as a probe pulse. All of the three pulses were intrinsically synchronized, made to overlap in space, and focused by a high numerical aperture (NA~1.25) objective lens. In the detection arm, we used a high numerical aperture (NA~0.9) condenser followed by a diffraction grating and a set of bandpass filters. This permitted efficient detection of the signal of interest on the background of other signals generated within the focal volume. A photomultiplier tube (PMT) with high gain and quantum efficiency (Hamamatsu model #R10699) was used to detect anti-Stokes signal photons at selected wavelengths. The PMT current output was digitized by a high-speed data acquisition card. Using this experimental arrangement, we can routinely detect CARS signals versus probe pulse delay times within five decades. The corresponding total power on the sample from the three beams does not exceed 15-20 mW. Other details and characteristics of the set up are described in our most recent work [20]. Figure 2

(a) demonstrates sensitivity and the attainable time resolution using the experimental arrangement. In addition, using theoretical algorithms and owing to the experiment's great sensitivity, we can retrieve the vibrational system's response function and Raman spectra for several vibrational modes. The flux-grown KTP crystal used in the experiment was cut at ϕ=40° and θ=**9**0°. Polarizations of all the three beams were made parallel and aligned in XY-plane of the crystal. Thus, technically, all the four symmetry tensor components [10,11] are involved in Raman mode excitation and scattering processes during CARS.

Lattice dynamics in condensed matter is modeled as time-dependent behavior regarding the expectation value of molecular/atomic displacement amplitude under a driving force. This driving force consists of a pair of pulsed fields with an optical frequency difference matching the energy of vibration quanta [23-25]. Quantitatively, the scattering signal at anti-Stokes frequency ($S_{as}(t_d)$) can be expressed as the following:

$$S_{as}(t_d) = \zeta_0 \int_{-\infty}^{\infty} |\vartheta(t)|^2 \varepsilon_{pr}^2 (t - t_d) dt \qquad (1).$$

In the above equation, $\vartheta(t)$ and $\varepsilon(t)$ are normalized time-dependent envelopes for atomic displacement amplitude and probe pulse, respectively. This also implies that ζ_0 represents detected anti-Stokes signal at a zero delay. The ensemble averaged displacement amplitude is negligible well before the arrival of the driving pulse pair and one can find a solution for the dynamics equation in the form of correlation integral:

$$\vartheta(t) = \int_{-\infty}^{\infty} g(t' - t)\varepsilon_1(t')\varepsilon_2(t')dt' \qquad (2).$$

In the equation above, $g(t)$ represents the response function of the corresponding

vibrational system to δ-pulsed driving fields. Both equations are of Fredholm type-I and can be solved using the Fourier transform method [26]. This is ensured by the correlation integral theorem and the fact that spectra and/or envelopes of $\varepsilon_1, \varepsilon_2, \varepsilon_{pr}$ pulses are known and can be measured. In the case when $\vartheta(t)$ is a real function, the response function *g(t)* and its Fourier transform can be ultimately obtained. The condition holds true for many types of vibrational systems that do not involve diffusional phase shifting events. As a consequence, precise spectra and fine features in the vicinity of Raman active vibrations can be effectively resolved. Figure 2 (a) shows an experimentally measured CARS signal versus delay time in the KTP crystal (open circles) under conditions that favor a coherently driven high-frequency (21.3 THz or ~710 cm^{-1}) Raman mode. For this case the OPO wavelengths were tuned to 1020 nm and 1098 nm respectively. The coherently driven Raman mode belongs to a main symmetric Ti-O bond stretching vibrations $(\nu_1(A_{1g}))$ within the distorted TiO_6 octahedra. The vibration has a relatively high damping rate so that the corresponding CARS signal decay time (~250 fs) is comparable with pulsewidths used in our experiments. The crystal is of high quality and the only mechanism that results in the CARS signal decreasing versus time delay, is a decay of the coherently driven phonon into phonons of lower energy. From the measurement, a crude estimate can be made for the phonon lifetime ($T_1 \cong 495$ fs) and the corresponding phonon line bandwidth in ($\Delta\nu = 1/\pi c T_1 \cong 21$ cm^{-1}). A more rigorous analysis that concerns spectral domain information retrieved from the time-domain data is needed. For this particular case, the excitation and probe pulses can not be considered as δ-functions ($t_p \sim 3 \times T_1$) and an approach reported earlier by our group, described in Ref. [27], yields in somewhat

distorted spectral data. Thus, equations above need to be solved in order to retrieve Raman spectra along with the dispersion of the real part of the associated resonant third order nonlinearity ($\chi^{(3)}(\omega)$). The Fourier transform ($S_{as}(\omega)$) of the measured time-dependent CARS signal is a first step in solving the equations. The corresponding result is shown in Figure 2 (b). The spectrum is smooth, as high-frequency noise in the time-domain CARS signal has a relatively low spectral power density and is not visible on linear scale. The main characteristic of the spectrum is a broadband and high-intensity pedestal, associated with ultrafast signal rise-time. The pedestal masks a narrower spectral feature. The latter may reflect a slower decay rate due to the phonon decay process mentioned above. Knowing the measured probe pulse spectrum, $(I_{pr}(\omega)=FT(\varepsilon_{pr}^{2}(t))$, and applying the inverse Fourier transform operation, allows the collection of time-domain data on the coherent displacement amplitude ($\vartheta(t)$) at $|\vartheta(t)|^2 = FT^{-1}\left(\frac{S_{as}(\omega)}{I_{pr}(\omega)}\right)$. Further, having $\varepsilon_1(\omega), \varepsilon_2(\omega)$ available from OPO pulse autocorrelation and spectral measurements and a Fourier transform of $\vartheta(t)$, one can arrive to resonant third order nonlinearity ($\chi^{(3)}(\omega)$) spectra contained in real and imaginary parts of $g(\omega)$. Figure 2 (c) shows the retrieved coherent amplitude function ($\vartheta(t)$) and the real and imaginary part of the resonant third order nonlinearity (Fig 2(d)) in the vicinity of the coherently driven $\nu_1(A_{1g})$ -phonon mode. The main peak's asymmetry is caused by the presence of two components with relative amplitude ratio of 26:11, bandwidths (FWHM) of 17.2±0.7 and 24±1.2 cm^{-1} and an energy separation of 16 cm^{-1} for the doublet. The difference in the bandwidths is explained by different damping rates for in-plane and along long axis vibrations within the TiO_6 octahedron [10]. A third component is also pronounced in the spectra with a position shifted to

lower energies by 65 cm^{-1}. This mode has a different symmetry and represents $v_2(E_g)$ anti-phase stretching vibration within TiO_6 octahedra. The peak can be better resolved under condition when one of the OPOs is detuned to provide more efficient coherent excitation for the $v_2(E_g)$ mode. As a result, the time-dependent CARS signal exhibits a more pronounced quantum beats pattern. Using this arrangement, the spectral bandwidth of the $v_2(E_g)$ mode was determined to be 21.3±0.7 cm^{-1}. The obtained parameters for the main $v_1(A_{1g})$ doublet and for the $v_2(E_g)$ modes are in good general agreement with the referenced reports [10,11]. We must note, however, that consistent bandwidth and Raman shift data for the doublet components could not be found throughout Raman spectroscopy characterization studies of KTP crystal published in the past [10-18, 28-31]. The result of fitting imaginary part of the resonant third order nonlinearity (i.e. Raman spectrum) using Lorentz-shaped multi-peak curves is also shown in Fig. 2(d) by solid lines with individual line details provided in the figure caption.

An unassigned phonon mode centered at ~820 cm^{-1} is perhaps a better example of the complex nature of Raman active vibrations in the crystal. Figure 3 (a) shows a CARS transient obtained for this case. The overall signal behavior shows quantum beats of at least two spectral components on the background of characteristic exponential decay with a noticeably longer time constant than for the $v_1(A_{1g})$ mode. Modeling of the time-domain behavior of CARS signals and the fitting of the experimental data require certain assumptions and use of multi-parametric fitting algorithms that do not have global minima. We have instead analyzed the obtained data by the approach that was outlined above. Fourier analysis of the signal

unequivocally reveals a presence of a strong nonresonant signal on the background of weaker contributions from the clustered phonon mode. This proves the fact that the mode is noticeably weaker in its intensity when compared to the $\nu_1(A_{1g})$ and $\nu_2(E_g)$ modes. Retrieved Raman spectra ($\mathrm{Im}(\chi^{(3)}(\omega))$) and data for the real part of the third order nonlinearity are shown in Figures 3 (b) and 3 (c) respectively. Three spectral components are involved in this case. They have energy separations of 18 cm^{-1} and 46 cm^{-1} and the values are in relatively good agreement with spontaneous Raman scattering measurements. The latter provide the range of 20.4-29.0 cm^{-1} and 34.6–39.2 cm^{-1} for the corresponding two parameters [11]. Spectral component bandwidths obtained from our data are 9.1±0.4 cm^{-1}, 7.5±0.6 cm^{-1} , and 11.2±0.5 cm^{-1} for the three components compared to ranges of 10.2-12.6 cm^{-1}, 9.2-10.8 cm^{-1}, and 14.0-16.4 cm^{-1} respectively reported by spontaneous Raman spectroscopy study [11]. The spread for both parameters is dependent on particular experimental conditions (e.g. crystal axes orientations with respect to laser polarization) when different scattering tensor elements have been accessed within the measurements. And finally we report a component amplitude ratio of 46:5:31. The value is not available for comparison from spontaneous Raman spectroscopy studies Phonon line bandwidths are approximately two times narrower (i.e. the corresponding phonon decay rate is two times lower) when compared to the high frequency modes ($\nu_1(A_{1g})$ and $\nu_2(E_g)$) that are stronger in Raman scattering. We explain this by the fact that the latter modes have a variety of efficient overtone or combinational phonon decay channels within either of the TiO_6 or PO_4 groups, resulting in lower energy vibrations. Therefore, we think, that based on the fact that the investigated ~820 cm^{-1} mode has a significantly lower

damping rate, the mode is not a vibration originating from either of the two main atomic groups and it is rather within Ti-O-P intergroup vibrations. The complex structure (i.e. presence of the triplet line) can be explained by shifted frequencies for vibrations of different symmetry within the group. Lower phonon damping rates (i.e. higher effective dephasing time $T_2^*=T_1$) makes up to a certain degree for the difference in the steady state SRS gain between the relatively weak mode at 820 cm^{-1} and the strong $\nu_1(A_{1g})$ and $\nu_2(E_g)$ vibrations. By using proper crystal orientation, it is possible to produce in SRS experiments (Stokes and anti-Stokes scattering) a nearly equal intensity and equidistant comb of frequencies that includes ~820 cm^{-1} mode. The comb can be used for ultrafast waveform synthesis.

In conclusion, we have demonstrated, using femtosecond time-domain coherent anti-Stokes Raman scattering spectroscopy, a resolution of complex Raman active vibrations in KTP crystal. The Raman spectra retrieved from our measurements show several spectral components corresponding to vibrations of different symmetries with distinctly different damping rates. Relative amplitude ratio, energy shifts, and bandwidths for an unassigned optical phonon mode triplet centered at ~ 820 cm^{-1} have been reported. The mode is thought to belong to vibrations in the Ti-O-P intergroup within the crystal. Results of our experiments can be used to estimate stimulated Raman gain for different vibrational modes in the crystal.

Authors acknowledge funding support from NSF (DBI-135530). A. Card and M. Mokim have contributed to this work equally.

References:

[1]X. D. Wang, P. Basseras, R.J.D. Miller, H. Vanherzelle, Appl. Phys. Lett. **59**, 519 (1991).

[2]Savatinova, I. Savova, E. Liarokapis, C.C. Ziling, V.V. Atuchin, M.N. Armenisek, V.M.N. Passrok, J. Phys.D: Appl. Phys. **31**, 1667(1998).

[3]V. Pasiskevicius, A.Fragemann, F. Laurell, R. Butkus, V. Smilgevicius, A. Piskarskas, App. Phys. Lett. **82**, 325(2003).

[4]V. Pasiskevicius, C. Canalias, F. Laurell, , App. Phys. Lett. **88**, 041110(2006).

[5]Y.F. Chen, Opt. Lett. **30**,400 (2005).

[6]L.L.Losev, J. Song, J.Xia, D. Strickland, and V. Brukhanov, Opt. Lett. **27**, 2100 (2002)

[7]M. Zhi, A. Sokolov, Opt. Lett. **32** , 2251 (2007).

[8]E. Matsubara, T. Sekikawa, and M. Yamashita, App. Phys. Lett. **92**, 071104 (2008).

[9]S. Baker, I. Walmsley, J.W.G. Tisch, and J.P.Marangos, Nature Photonics **5**, 664 (2011).

[10]G. E. Kugel, F. Brehatt, B. Wyncket, M. D. Fontanat, G. Marniers, C. Carabatos-Nedelect, J. Mangin, J. Phys. C: Solid State Phys. **21,** 5565(1988).

[11]G.H. Watson, J. Raman Spectrosc. **22**, 705 (1991).

[12]K. Vivekanandan, S. Setvasekarapandian, P. Kolandaivel, M.T. Sebastian, S. Suma, Mater. Chem. Phys. **49**, 204 (1997).

[13]G.A Massey, T.M. Loehr, L.J. Willis, J.C. Johnson, Appl. Optics **19**, 4136 (1980).

[14]V.M Garmash, D.N. Govorun, P.A. Korotkov, V.V Obukhovskii, N.I. Pavlova, I.S Rez, Opt. Spectrosc. **58**, 424(1985).

[15]G.A. Kourouklis, A. Jayaraman, A.A. Ballamn, Solid State Commun. **62**, 379 (1987).

[16]Y.K. Voronki. V.A. Dyahov, A.B. Kudryavtsev, V.V. Osiko, A.A. Sobol, E.V. Sorokin,Sov.Phys.-Solid State **31**, 1736 (1989).

[17]S.Fursawa, H. Hayasi, Y. Ishibashi, A. Miyamoto, T.Sasaki, J.Phys.Soc.Jpn. **60**, 2470 (1991).

[18]C.S. Tu, A.R. Guo, R. Tao, R.S. Katiyar, R. Guo, A.S. Bhalla, J. Appl. Phys. **79**, 3235 (1996).

[19]S.Yang, R.Wysolmerski, and F. Ganikhanov, Opt. Lett. **36**, 3849(2011).

[20]S.Yang, S.Adhikari, L. Zhang, R.Wysolmerski, G, Spirou, and F. Ganikhanov, Appl. Phys B: Lasers and Optics **111**, 617(2013).

[21]K.Bhupathiraju, A.Seymour, F.Ganikhanov, Opt. Lett. **34**, 2092 (2009).

[22]J.Rowley, S.Yang, F. Ganikhanov, J. Opt. Soc. Am. B **28**, 1026 (2011).

[23]A. Laubereau, D. von der Linde, and W. Kaiser, Phys. Rev. Lett. **28**, 1162 (1972).

[24]A. Laubereau and W. Kaiser, Rev. Mod. Phys. **50**, 607 (1978).

[25]S. A. Malinovskaya, Opt. Lett. **33**, 2245(2008).

[26]A.Jerry, *Introduction to Integral Equations With Applications*, (2d edition, John Willey and Sons, Inc.,1999)

[27]S. Yang, F. Ganikhanov, Opt. Lett. **38**, 4754 (2013).

[28]Ch. Ferrer, A. Segura, M.V. Andres, V. Munoz, J. Pellicer, J. App. Phys. **79**,3200 (1996).

[29]X. Liwen, C. Dawei, N. Hongda, Chinese Phys. Lett. **1.6**,225 (1989).

[30]M.J. Bushiri, V.P. M. Pillai, R. Ratheesh, V.U. Nayar, J. Phys. Chem. Solids **60**, 1983 (1999).

[31]M.J. Bushiri, V.U. Nayar, J. Nonlinear Optic. Phys. Mat. **10**, 345 (2001).

Figure 1.

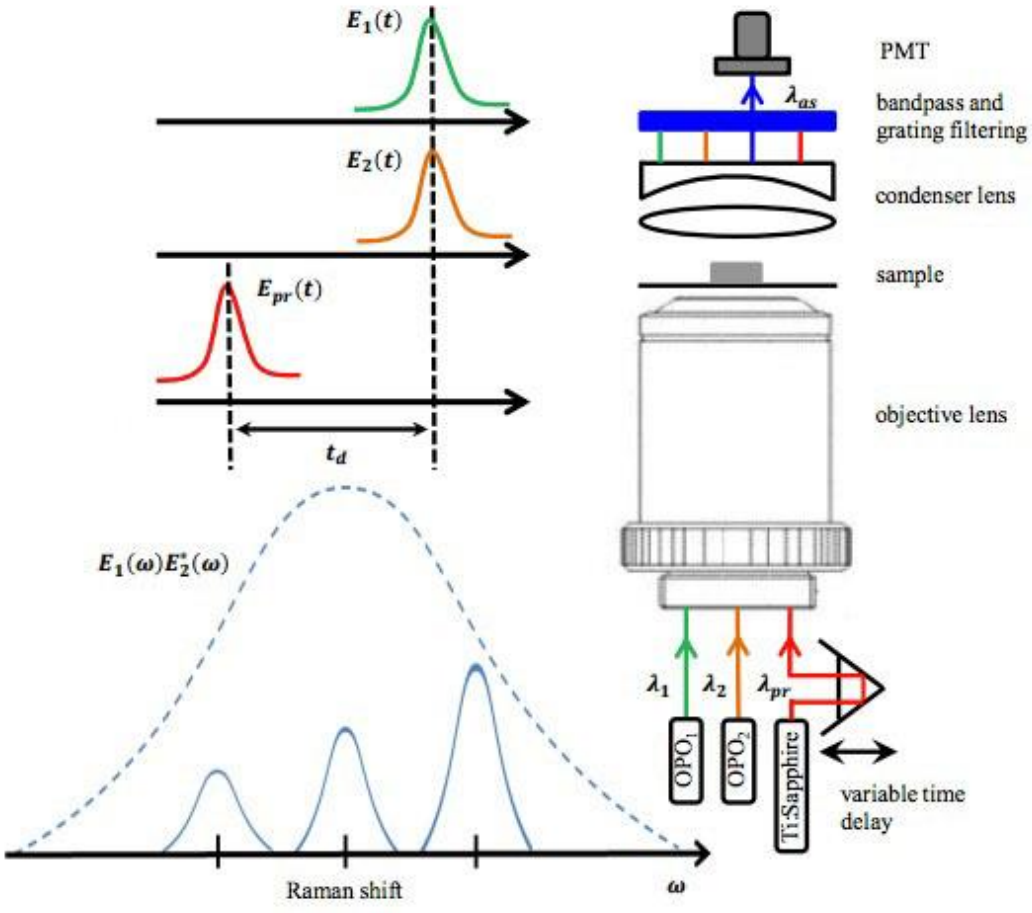

Experimental diagram and layout for three-color time-domain CARS spectroscopy experiments that employ tunable optical parametric oscillators. Pair of transform-limited 110-150 fs pulses at $\lambda_1$and λ_2 wavelengths are used to coherently drive Raman active vibrational modes in the vicinity of corresponding ω_1-$\omega_2$frequency shifts. A pulse at λ_{pr}=765 nm is time delayed and probes the resulting coherent excitation at different delay times. CARS transients at anti-Stokes frequency are detected within five orders of magnitude. Polarizations of all the three beams were made parallel to each other and aligned either along X- or Y-axis of the KTP crystal under study.

Figure 2.

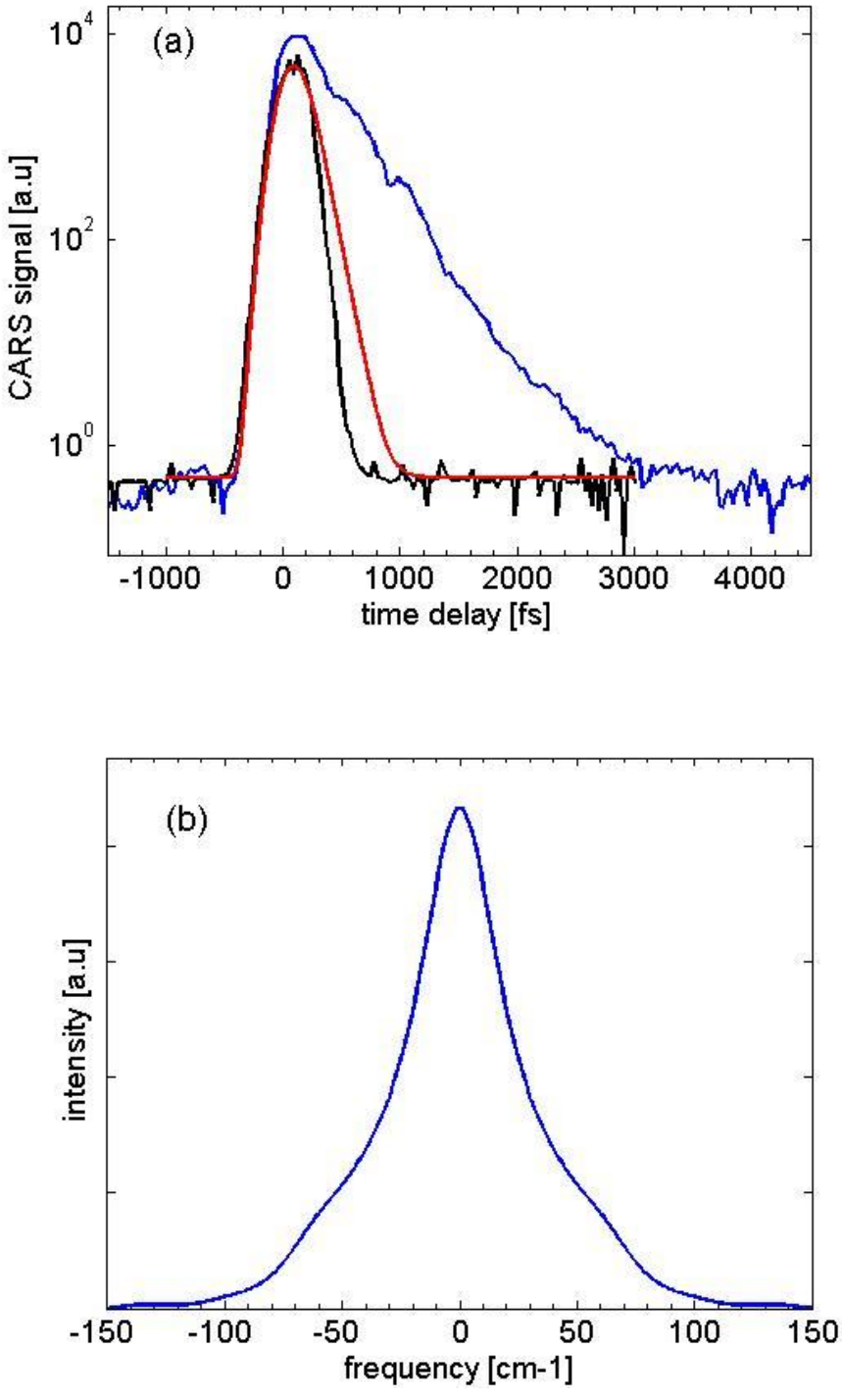
(a)
CARS signal [a.u]
10^4
10^2
10^0
-1000
0
1000
2000
3000
4000
time delay [fs]
(b)
intensity [a.u]
-150
-100
-50
0
50
100
150
frequency [cm-1]

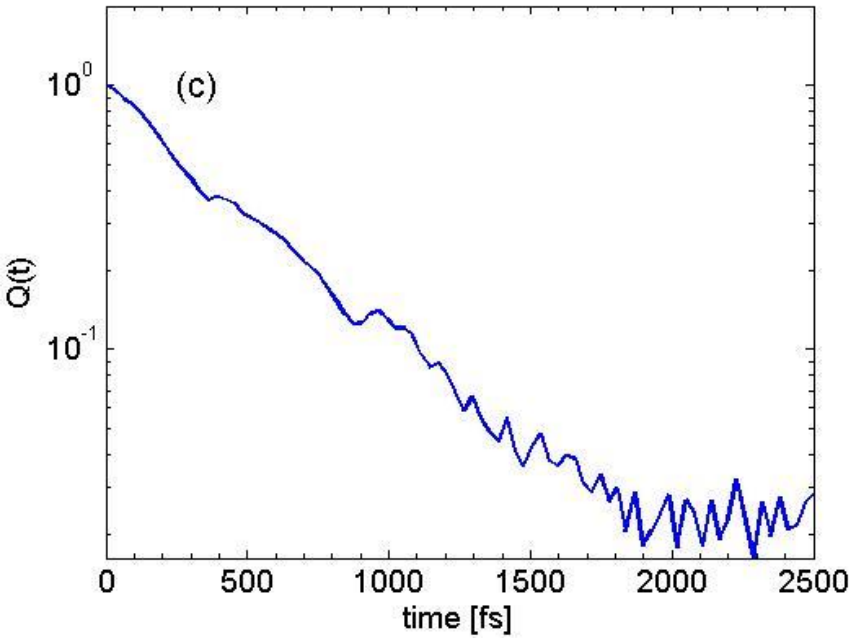

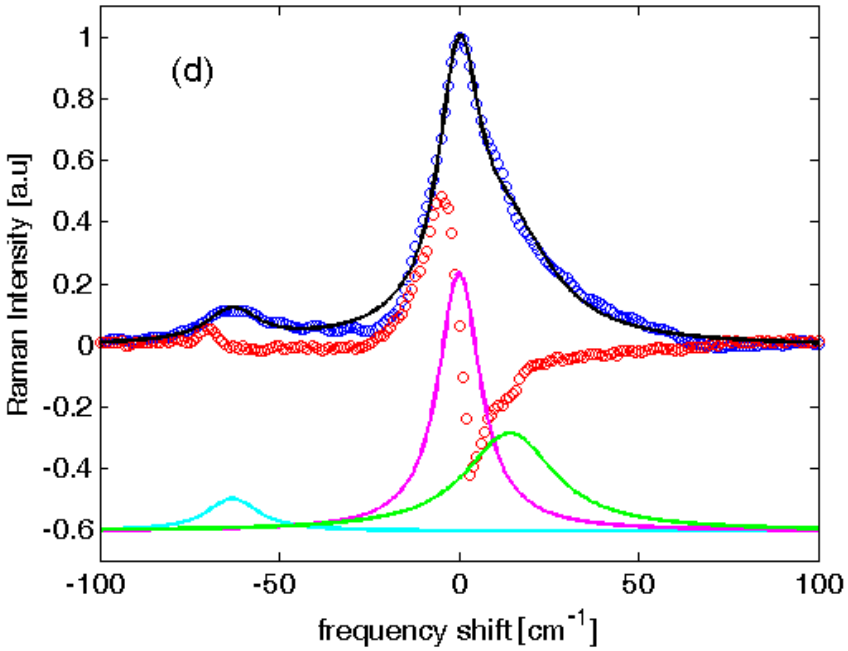

Time-domain CARS system instrument response obtained in quartz glass (black curve). Simulated CARS transient for Raman active vibrational mode with dephasing time T2=150fs (red curve). CARS transient detected in KTP crystal under the conditions specified below (blue curve). The broadband OPO pulses were tuned to

1020 nm and 1100 nm center wavelengths to coherently drive the main ν_1 (A1g) high frequency Raman active mode at ~700 cm-1. (b) CARS signal spectrum ($S_{as}(\omega)$) showing a narrower spectral feature on the background of a broadband pedestal corresponding to the transient signal's fast rise time. (c) Time-domain response function (g(t)) that was obtained by solving equations (1) and (2) using Fourier transform method. (d) Dispersion of real (red open circle) and imaginary (blue open circles) parts of the resonant third order optical nonlinearity ($\chi^{(3)}(\omega)$) in the vicinity of the coherently driven Raman active modes. The part corresponding to Raman spectra (i.e. Im$\chi^{(3)}(\omega)$) is also shown fitted with solid black curve representation a sum of three Lorentz-shaped envelopes with bandwidths of 21 cm^{-1} , 17 cm^{-1} , and 25 cm^{-1} starting from the red shifted ν_2 (E_g)–mode (cyan color peak).

Figure 3.

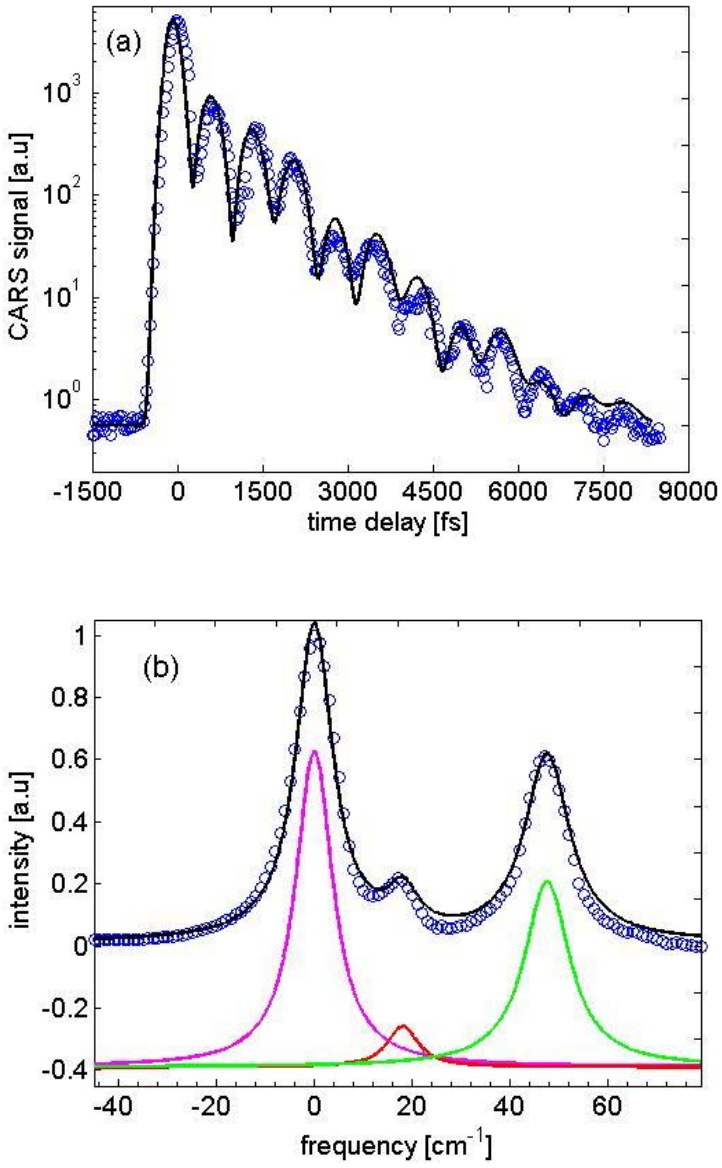

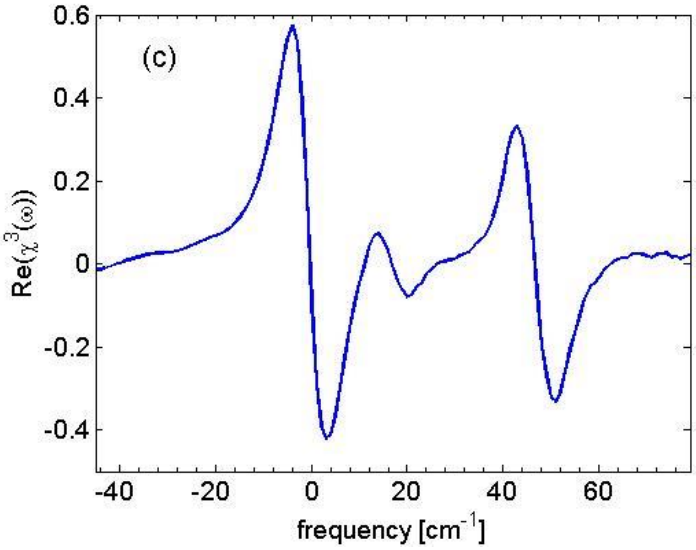

(a) CARS transient (blue circles) obtained from KTP crystal when unassigned Raman active vibrational modes at ~820 cm^{-1} are coherently driven and probed. A proper wavelength combination was chosen for the OPOs (λ_1=967 nm and λ_2= 1051 nm) so that the corresponding shift is targeted at its center. Simulated CARS signal (black curve) obtained under amplitude, damping rate, spectral shift parameter values for the vibrational modes using retrieved Raman spectra data. (b) Retrieved Raman spectra (blue curve), simulated Lorentz-shape curves for the three spectral components that yield in cumulative fitting curve (black). (c) Corresponding real part of the third order optical nonlinearity.

MANUSCRIPT- 3

Published in Applied Physics Letters, October 2017

Tracing molecular dephasing in biological tissue

Mohammad Mokim, Chris Carruba and Feruz Ganikhanov

Department of Physics, University of Rhode Island, 2 Lippitt Road, Kingston, RI, 02881.

Corresponding Author: Feruz Ganikhanov, Ph.D.

Department of Physics

University of Rhode Island

East Hall, 2 Lippitt Road

Kingston, RI, 02881, USA

Phone: 401.874.2633

Email address: fganikhanov@uri.edu

We demonstrate the quantitative spectroscopic characterization and imaging of biological tissue using coherent time-domain microscopy with femtosecond resolution. We identify tissue constituents and perform dephasing time (T_2) measurements of characteristic Raman active vibrations. This was shown in subcutaneous mouse fat embedded within collagen rich areas of the dermis and the muscle connective tissue. The demonstrated equivalent spectral resolution (<0.3 cm^{-1}) is an order of magnitude better compared to commonly used frequency-domain methods for characterization of biological media. This provides with the new dimension and parameter in biological media characterization and can become an effective tool in detecting minute changes in bio-molecular composition and environment that is critical for molecular level diagnosis.

Fundamental nonlinear optical phenomena have been shown to be useful in applications related to noninvasive characterization of biological media [1-4]. Raman scattering based techniques, both spontaneous and coherent versions, are of particular interest since their spectroscopic power can deliver molecular sensitive information that can become a key in early diagnosis of diseases. Absolute majority of the relevant applications of the techniques is, for natural reasons, in frequency domain. The coherent Raman microscopy studies were primarily applied to highlight tissue and cells constituent by producing high-contrast images at targeted Raman active vibration [5,6]. Spontaneous Raman version has been applied with greater focus towards detection of spectral features within cells and tissue [7]. However, the reported results have been limited to obtaining characteristic multi-line spectra and detecting relative changes in the intensities and spectral shifts with a goal to correlate those with

biomolecular alterations occurring on sub-cellular level [8]. The true spectroscopic strength, that would ultimately include resolution of molecular vibration damping rates Γ (or linewidths, $\Delta\nu=1/\Gamma$) and line shapes, has not been enabled and demonstrated. It is worth noting that the damping rate is directly affected by inter- and intra-molecular interactions. Therefore, ability to measure Raman line shapes with a precision is absolutely crucial from that point of view. Depending on the immediate molecular environment (e.g. density, viscosity) and composition of tissue and cells, linewidths for the investigated Raman active modes can vary broadly. For instance, in aqueous solutions solute-solvent interactions can result in linewidth range of 0.3-7.5 cm^{-1} dependeding on the molar ratio [9]. Both spontaneous Raman and frequency-domain have the best possible resolution of ~ 3-7 cm^{-1}. The limits are imposed by the detection sensitivity in spontaneous Raman spectroscopy. Laser pulse bandwidths (~3-10 cm^{-1}) employed in coherent Raman microscopy does not provide a better resolution either. In addition, for the latter case the need to adjust laser wavelength in point-by-point spectral measurements adversely impacts the spectral resolution and precision. As a result, it becomes impossible to measure and detect Raman line shapes and bandwidths with a desired precision.

An alternative to the frequency-domain Raman scattering techniques is time-domain Coherent Anti-Stokes Raman Scattering (t-d CARS) spectroscopy. CARS signal can be viewed as a result of scattering of a probe pulse with amplitude E_{pr} on the coherence built in the material. The initial coherence is the result of individual molecular displacements (q_i) being phased in by the excitation pair of pulses (E_1, E_2) with the difference frequency (ω_1-ω_2) matching Raman active vibration (ω_R). The

action results in macroscopic coherent amplitude (*Q*). The coherence starts to decay freely in time as the consequnce of various inter- and intra-molecular interactions that lead to changes in the phase (pure dephasing) and amplitude of the individual vibrations. Ensemble averaged solution for *Q* contains autocorrelation function that yields in $\langle q(t)q(t')\rangle = exp(-|t-t'|)/T_2$ for the case of phase changing collisions that dominate the interactions. Constant T_2 represents characteristic dephasing time and the Raman active line is homogeneously broadened with the linewidth of

$$\Delta\gamma = {}^{1}/_{\pi c T_2} \qquad (1),$$

expressed in wavenumber units.

The CARS signal is detected at anti-Stokes frequency$\left(\omega_{as} = \omega_{pr} + \omega_1 - \omega_2\right)$. Non-resonant background can be more efficiently suppressed in t-d CARS down to the level of detector's dark which is different from the case of a coherent frequency-domain method. This gives an opportunity to detect really weak Raman active lines and potentially the ones that cannot be detected by spontaneous or coherent Raman spectroscopy. Tracing t-d CARS signal at longer delays (i.e. slower resonant part) within a decade translates to better than few percent precision in T_2 ($\Delta\nu$) measurements [10]. In other words, t-d CARS can result in the Green's function (*G(t)*) for the molecular system as a response to the ultrashort ($E_1(t)$,$E_2(t)$)–pulse excitation. An ability to measure (*G(t)*) on extended time scale and within high dynamic range provides much more fine information about the corresponding Raman lineshape [10]. Lower limit for the equivalent spectral resolution is determined by one's ability to trace t-d CARS signal for as long time delays as possible.

The goal of this work is the first direct dephasing time (T_2) measurement of specific molecular vibrations within biological tissue. Another novelty is that we demonstrate detection of time-domain replica within biological tissue, traced within more than one decade, for important and previously unresolved Raman signature line within fat cells. The ability to measure the corresponding dephasing times with high precision resulted in equivalent spectral resolution of better than 0.3 cm^{-1}. This constitutes another important point since the achieved resolution is an order of magnitude better than the one that can be ultimately achieved by frequency-domain approaches applied to tissue or cell characterization. These highlight the strong potential of the time-domain approach with regard to biochemical and biomedical applications that seek reliable molecular level indicators for early disease diagnosis, etc. The only demonstration of the time-domain CARS microscopy showed lower sensitivity and was limited to artificial structures like polysterene beads probed at much stronger Raman resonance [11].

The ultrashort pulses (E_1,E_2) are provided by independently tunable (960-1120 nm) optical parametric oscillators (OPO) running at 76 MHz [12]. A small part of femtosecond Ti:sapphire laser output, that simultaneously pumped the OPOs, served as a third color pulse (E_{pr}) that can be delayed. The three pulses are intrinsically synchronized in time.

For the case of biological tissue, generated SHG and CARS signals are detected in backward direction. SHG and CARS signals were filtered by the appropriate bandpass filter (BP) and diffraction grating (GR) with 1200 grooves/mm. The cooled PMT detector has a gain of up to 10^7, high cathode sensitivity, and a dark

current below 1 nA. The detected signal was digitized by data acquisition card. The card also provided synchronized analog signals to drive x-y galvo-scanners in order to generate raster scans for imaging. SHG and time-delayed CARS images can be generated with a spatial resolution of 300 nm using high-numerical aperture (NA=1.2) objective.

The tissue samples used in this investigation were dissected from above the *longisimus dorsi* muscle of C57BL/6 mice under after euthanasia with outer and inner surfaces of the adipose tissue identified. Slices of up to 100 μm in thickness were fixed for 1 hr in 4% PFA at 3°C. The coverslips were treated with gelatin-chromium potassium sulfate solution for optimal tissue contact.

Fig.1 (a) shows a SHG image obtained with scanned fundamental beam, at optical frequency ω_2, delivered by one of the OPOs tuned to ~1095 nm. The image shows a high SHG signal within the collagen type-II rich areas within the dermis and connective muscle tissue for which the second order optical nonlinearity is strong due to the lack of inversion center in the molecular structure of this type of protein.

There are fairly large areas in between the collagen areas where the SHG signal is absent. The collagen bundles could sustain 30-40 mW average power levels at this wavelength in the scanning mode of 2 frames/sec without the collagen fibrils being visibly altered or damaged. With the focused beam fixed on one spot within the collagen rich area a detectable damage could occur within the timeframe of few minutes. Figure 1(b) shows CARS image of the same area at zero time delay. The OPO wavelengths were tuned to 978 nm and 1095 nm respectively so that the targeted Raman active mode is at a frequency shift of ω_1-$\omega_2 \approx$ 1072 cm^{-1}. Some collagen

bundles seen in Fig. 1(a) can be still fairly well identified on the CARS image. However, the contrast is significantly lower with respect to surrounding areas. The image shows very strong signals coming from the areas where SHG signal was absent. These parts are filled with dense mouse fat as this was further confirmed by time-domain CARS measurements. Unlike the collagen, the structure of the fat molecules is centro-symmetric and therefore the areas with the fat are not seen on the SHG image. The CARS image clearly resolves a blood vessel with red blood cells (RBC) that does not have any trace in the SHG image. CARS and SHG images complement each other in a useful way. SHG imaging modality helped in positioning of the sample so that the other two beams can be blocked to minimize the risk of damage while we were identifying parts of tissue to be characterized. CARS image shown in Fig. 1(c) was obtained when the probe pulse was delayed by 200 fs (t_d=200 fs) with respect to the excitation pair. Both b) and c) images rather display frequency unspecific non-resonant CARS background. Indeed, the contrast ratio between fat tissue part and the remaining background remains about the same with a maximum value of about factor of 2.8. When the delay is further increased beyond 500 fs the contrast drastically improves and the ratio of CARS signal within the fat tissue and the surrounding areas can exceed an order of magnitude [Fig. 1(d) and 1(e)].

Fig. 2(a) shows CARS signal versus delay time when Raman active vibrations within ~1075cm^{-1} vicinity were targeted. For this case the scanning area was reduced (~20x20 μm^2) to match large piece of fat located at around the center of the image shown in Fig 1(b). Signal fluctuations are fairly high and the signal-to-noise ratio is about factor of 5 despite the fact that the data were effectively averaged across more

than 4000 pixel area. The data quality degraded further if the scanning was not performed and this has been the case for fairly moderate (i.e. <25 mW in combined power for the three beams) average power levels focused into the fat area. Some observations indicate that the tissue samples have been altered due to accumulated excess heat and high peak powers that lead to molecular ionization. The detailed study on this issue has not been performed. The obtained CARS transient clearly shows at least two spectral components that result in the coherent beat signal. The decay time is fairly long (~2 ps) and there is an indication of different decay times for the components. This can be noticed in decreased modulation depth for the beat signal at longer time delays. The obtained transients have been further analyzed by generating theoretical curves to fit the experimental data. We have applied a model that is based on time dynamics of the macroscopic coherent amplitude (*Q*) [13]. Time-domain CARS signal can then be calculated by using the following formulae:

$$\boldsymbol{S_{as}(t_d)=\xi_0 \int_{-\infty}^{\infty} |Q(t)|^2 \varepsilon_{pr}^2 (t-t_d)\, dt} \qquad (2)$$

$$Q(t) = \int_{-\infty}^{\infty} G(t-t')\varepsilon_1(t')\varepsilon_2(t')dt \qquad (3).$$

In the equations above, $\varepsilon_{1,2,pr}(t)$ stand for unit area driving and probe pulses, ξ_0 - detected anti-Stokes signal at zero delay, *G(t)* - response (Green's) function of the corresponding vibrational system to δ-pulsed driving fields. Applying certain solution algorithms for the above Fredholm type-I equations the *G(t)* can be retrieved for arbitrarily shaped pulses [8]. We can also seek solution for *G(t)* function for our case of i) Gaussian pulses and ii) when molecular collisions dominate the dephasing process. As was discussed in the introduction, the latter condition represents the case

of homogenously broadened line. Therefore,

$$G(t) = h(t)\sum_j A_j e^{-t\left(\frac{1}{T_{2j}} - i\Delta\omega_j\right)} \qquad (4),$$

where *h(t)* is Heaviside step function, A_j – Raman line component amplitude, T_{2j} –the component's dephasing time, $\Delta\omega_j$ - the component's shift from reference frequency (e.g. from $(\omega_1\text{-}\omega_2)$). By varying the above parameters we can find the best fit to our experimental data. For the vibrational modes in the vicinity of $(\omega_1\text{-}\omega_2)\approx$1072 cm^{-1} the best fit corresponded to the presence of two vibration lines with a frequency difference of $\Delta_{12} = \Delta\omega_1 - \Delta\omega_2$ =28.7 cm^{-1}, dephasing times of 2.6 and 1.7 ps and the amplitude ratio of A_1/A_2=19:5 respectively. The dephasing times (T_{2j}) obtained from our measurements suggest, if we apply formula (1), that the two homogenously broadened vibrations have linewidths of $\Delta\nu_1 = 4.1$ cm^{-1} and $\Delta\nu_2$=6.3 cm^{-1}. Some comparison can be made with spontaneous Raman data available for fats [14,15]. We did not find any data on the relevant case that is obtained with a coherent frequency-domain technique. Spontaneous Raman spectroscopy of adipose tissue in mice has shown two not well resolved C-C bending vibrations within ~1060-1120 cm^{-1} range sitting on a broad shoulder [15]. The line separation within the doublet at around 1080 cm^{-1} is not reported and could not be inferred from the data. The two, strongly overlapping and merging lines, show the combined width of about 25 cm^{-1} which is about the separation Δ_{12}that we found using our data. Thus, our results represent first measurement of the linewidths and the spectral difference for the C-C vibrations in fat and clearly demonstrate the power of the time-domain method. Another feature that follows from our data is that the individual components with the doublet have different linewidth.

We next targeted higher-frequency and stronger line at ~1265-1275 cm^{-1}, assigned as a =C-H bending vibration, to get a better comparison with available spontaneous Raman studies since the line is better resolved in them. Fig. 3 shows the transient signal when Raman active vibrations at around ~1270 cm^{-1} frequency shift were excited and probed within the fat tissue. By fitting the data, using the model described above, we found that there are two closely spaced vibration modes at 1272 cm^{-1} with the frequency difference of $\Delta_{12}= \mathbf{48.5}$ cm^{-1}, dephasing times of 550 fs ($\Delta\boldsymbol{\nu_1} = \mathbf{19.3}$ cm^{-1}) and 670 fs ($\Delta\boldsymbol{\nu_1} = \mathbf{15.8}$ cm^{-1}) , and the amplitude ratio of 33:13. The study reported in [15] identifies this C-H bending doublet positioned at 1264 cm^{-1} and 1301 cm^{-1} resulting in a frequency spacing of 35-40 cm^{-1} with linewidths that could not be obtained from the data. The doublet line frequency differences show some agreement with the one detected in our experiments. As concerned the linewidths, our work is again the first to address and report that. Overall, none of the Raman studies that we found on fatty acids, proteins, DNA [16] provided explicit line bandwidths. This is presumably due to the limited (~3-7 cm^{-1}) spectral resolutions and low scattering signals. Thus, we find our data to be the first to reveal the more precise information on line separations and the only one available for the corresponding linewidths.

We have compared our results in mouse fat with identical time-domain CARS measurements that we performed in olive oil. Oils and lipids in fats have similar molecular composition and thus should have similar Raman active vibrational spectra. Raman active lines corresponding to C-C stretching vibration at ~1070 cm^{-1} and scissoring (C-H) modes at 1267 cm^{-1} [17] were targeted. The corresponding results are

shown in Fig. 4 (a) and (b). Since the data quality had been substantially better we were able to determine the parameters (see figure caption) more precisely. We point out again that a comprehensive comparison with data obtained by frequency- domain methods could not be performed since linewidths data were not available for the two modes in oil either. In general, from our experiments, fairly good agreement is found between fat and oil data as concerned linewidth and spectral separation parameters. However, the small differences, above spectral resolution, still noticeable. More detailed studies are needed, especially for different types of oils and fatty acids, in order to come up with a credible explanation for the detected differences. If we turn to the data for mouse fat again, one can see that there is a factor of 3-4 difference in linewidths for the targeted C-C and =C-H bending vibrations. We attribute this to the differences in character and lengths of the bonds and we think that those play a larger role in determining the dephasing times (damping rates, linewdith) for the vibrations compared to the heterogenous molecular environment.

In conclusion, we reported on implementation of spectroscopic imaging and characterization approach based on time-resolved version of CARS. We can identify tissue constituents and measure dephasing times for the associated vibrational modes. We show that the time-domain nonlinear microscopy of tissue delivers much more precise information on molecular fingerprints of the tissue constituents. Relating this type of information to diagnostics of diseases will be the task of major importance for future efforts.

Funding

Funding from NSF (DBI-1355307) is greatly appreciated.

References

[1]W. Denk, J.H. Strickler, and W.W. Webb, Science **105**, 73 (1990).

[2]P.J. Campagnola, and L.M Leow, Nat. Biotechnol. **21**, 1536 (2003).

[3]M. Zimmerley, P. Mahou, D. De´barre, M.Schanne-Klein, and E. Beaurepaire, Phys. Rev. X **3**, 011002 (2013).

[4]F.W. Christian, W. Min, B.G. Saar, S. Lu, G.R. Holtom, C. He, J.C. Tsai, J.X. Kang, and X.S. Xie, Science **322**, 1857 (2008).

[5]C.L. Evans, E.O. Potma, M. Puoris'haag, D. Cote, C.P. Lin, and X.S. Xie, Proc. Natl. Acad. Sci. U.S.A **102**, 16807 (2005).

[6]C.P. Pfeffer , B. R. Olsen, F. Ganikhanov , and François Légaré, J. Struct. Biol. **164**, 140 (2008).

[7] W. Liu, H. Wangc, J. Du, C. Jing, Biosensors and Bioelectronics **97**, 70 (2017)

[8] K. Eberhardt,C. Beleites, S. Marthandan, Ch. Matthäus, S. Diekmann, and J. Popp, Analytical Chemistry **89**, 2937 (2017)

[9] K. Tanabe, J. Hiraishi, J. Raman. Spectrosc. **12**, 274 (1982)

[10] A. Card , M. Mokim , and F. Ganikhanov, AIP Advances **6** , 025115 (2016)

[11]A.Volkmer, L.Book, and S.X. Xie, Appl. Phys. Lett. **80**, 1505 (2002).

[12]J. D. Rowley, S.Yang, and F. Ganikhanov, J. Opt. Soc. Am. B **28**, 1026 (2011).

[13]A. Laubereau, and W. Kaiser, Rev. Mod. Phys. **50**, 607 (1978).

[15] G. Dobson, Eur. J. Lipid Sci. Technol. **103**, 815 (2001)

[14]P. Meksiarun, B. B.Andriana, H. Matsuyoshi , and H. Sato, Sci. Rep. **6**, 37068 (2016).

[16] G.J. Thomas, Annu. Rev. Biophys. Biomol. Struct. **28**, 1 (1999)

[17]R. Korifi, Y. Le Dreau, J. Molinet, J. Artaud, and N. Dupuy, J. Raman Spectrosc. **42**, 1540 (2011)

Figure 1.

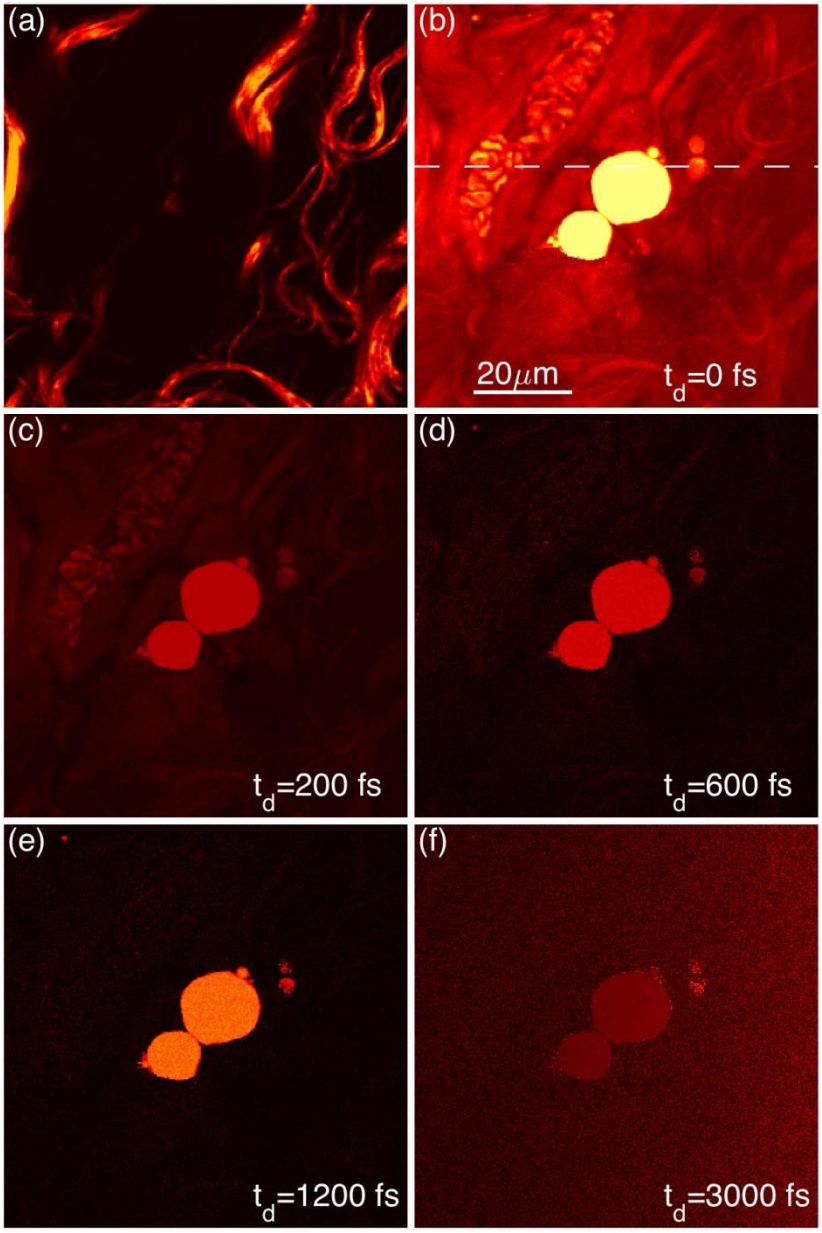

(a) SHG image obtained from the mouse dermis area; (b) CARS image of the same area at zero delay time between the probe (E_{pr}) and driving (E_1,E_2) pulses and ω_1-ω_2=1072 cm^{-1}. (c)-(f) CARS images at different delay times.

Figure 2.

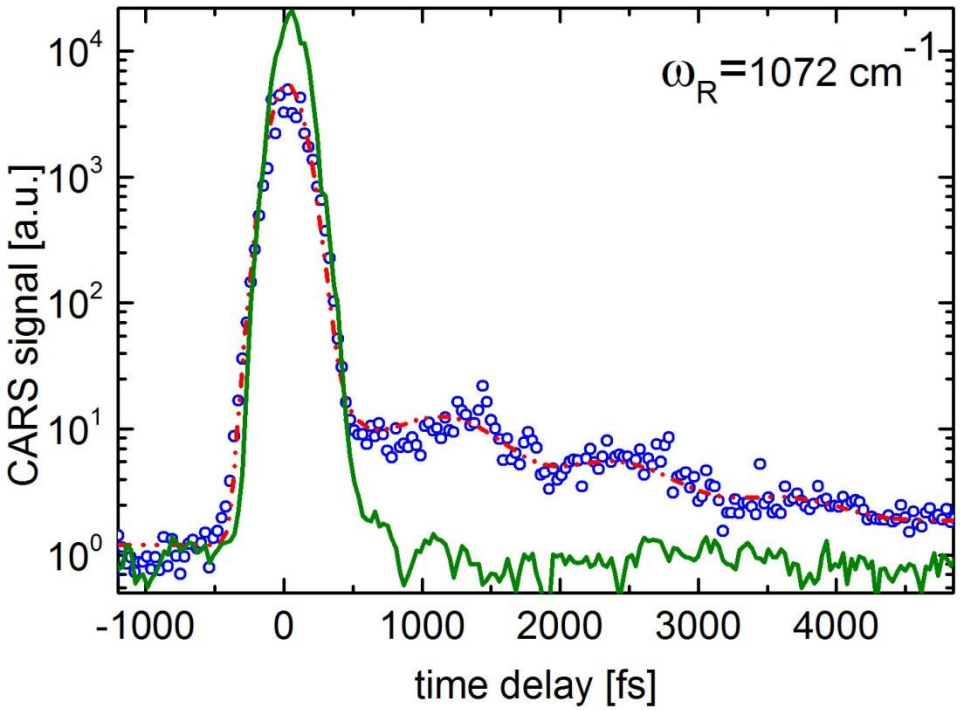

Time-domain CARS signal obtained from the ~16 μm diameter fat area located at the center of the mouse tissue for the image shown in Fig. 1(b). Solid green line represents non-resonant CARS signal obtained in microscope glass slide that was detected in the same (i.e. backward) direction and under the same other conditions. Dash dotted line represents the best fit to the data obtained by using formulae (2)-(4) and varying the corresponding line parameters (see text).

Figure 3.

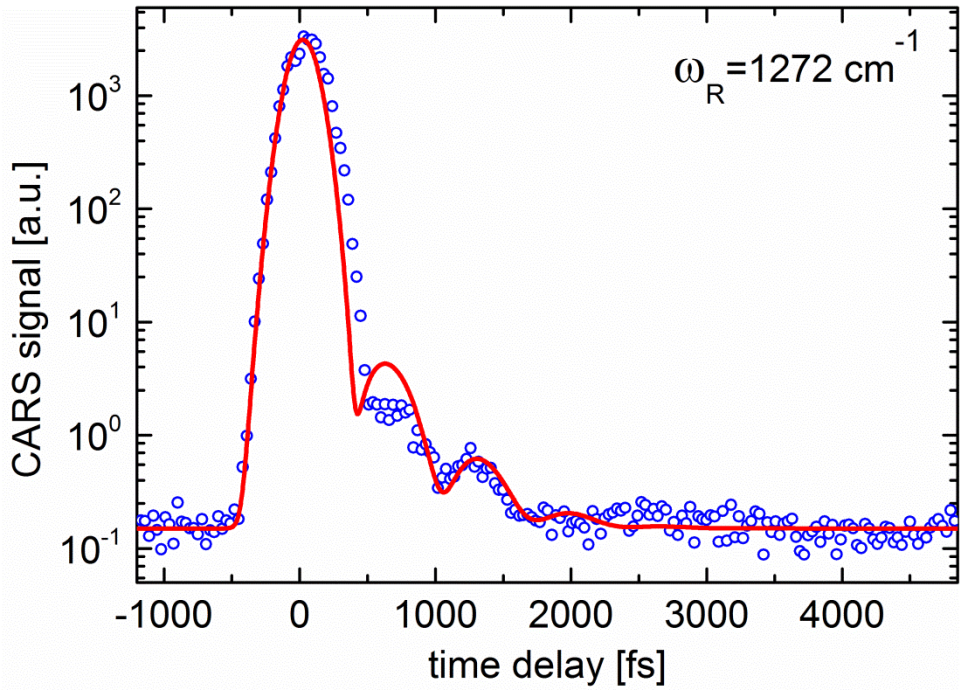

Time-domain CARS signal obtained from the mouse tissue area identified as a fat in the vicinity of Raman frequency shift of ≈1270 cm^{-1}. Solid line represents the best fit to the data obtained by using formulae (2)-(4) and varying the corresponding line parameters (see text).

Figure 4 (a), (b).

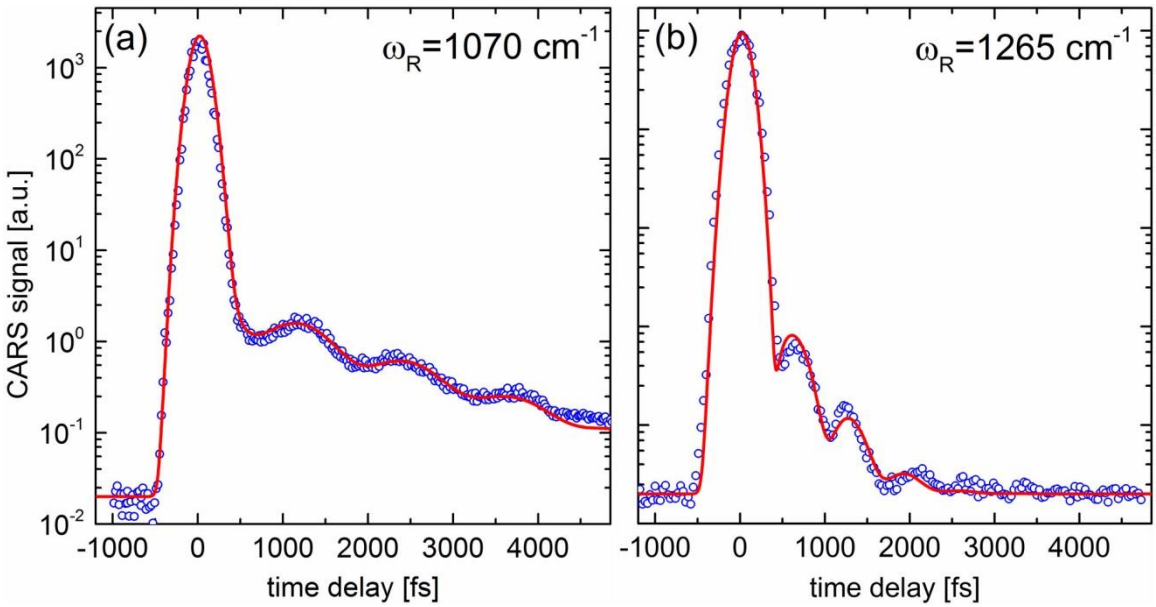

Time-domain CARS signals (open circles) obtained from a drop of olive oil. The Raman active vibrations near a) ≈1070 cm^{-1} and b) 1265 cm^{-1} were targeted and probed. The solid line represents the best fit to the data obtained using formulae (2)-(4) with the following parameters: (a) $\Delta\nu_1 = 3.7\ cm^{-1}, \Delta\nu_2 = 5.6\ cm^{-1}$, $\Delta_{12} = 23\ cm^{-1}$, A_1/A_2=13/3; b) $\Delta\nu_1 = 21.6\ cm^{-1}$, $\Delta\nu_2 = 17.5\ cm^{-1}$, $\Delta_{12} = 41.4\ cm^{-1}$, A_1/A_2=11/3.

APPENDIX

Detailed experimental procedure and alignment:

In this section, we will discuss the light sources at first, which is the pivotal part of the experiment, and then we will briefly describe the concept and set up of our two experimental techniques, Coherent Anti stokes Raman scattering (CARS) microspectroscopy and SHG microspectroscopy.

1. The sources of light:

Mode-locked Ti. Sapphire laser:

The main laser source we have used is the mode-locked ultrafast laser that uses Titanium: sapphire as the gain medium (Mira-HP, Coherent), tunable from 700 to 1000 nm. This laser is also pumped by another laser, green laser, with power 17W.The repetition rate (or frequency) of this laser is 76 MHz. The output power (~ 3-3.7 mW) of this mode-locked laser is then passed through the two cavity prism to compensate the pulse. A small portion of this pulse is out coupled through the side-port of the Glan-Taylor prism. The large portion of the beam, however, spilt into two equal parts, and used to synchronously pump the two OPOs. On the other hand, the small portion of the beam is used as probe pulse for CARS experiment.

Optical parametric oscillator (OPOs).

OPO-1.

The nonlinear gain media, allowing quasi-phase matching condition, for OPO1 is the stoichiometric lithium tantalate (PPSLT) nonlinear crystal, generating parametric

oscillation at the near IR-pump wavelengths in both for continuous wave (cw) and short pulse mode.

The crystal is 1 mm width, 0.5 mm thick, and 15 mm long-z cut that was pooled within 13 mm distance along the height. The grating period is varied from 17.50 to 24.80 micron with 0.6 micron differences between consecutive periods. The pump power is 1.15 mW, delivered by TiS mode-locked laser. The pump beam is focused onto the crystal by a 76 mm focal length lens. The OPO cavity is consist of two concave mirrors and three plane parallel substrate mirrors. A pair of Brewster cut angle prisms was used to compensate the dispersion. The optimal distance between the two prisms (apex to apex) was found to 280 mm in order to get the short pulses within the tuning range from 960 to 1050 nm. The pulse characteristics are shown in figure 1.

OPO-2

OPO2 is based on a periodically pooled lithium niobate (PPLN) nonlinear crystal. This OPO serves the wavelengths ranging from 1050 to 1100 nm.

Detailed OPOs characteristics and performance were reported in [1, 2]

2. Super continuum generation:

Supercontinuum generation was first observed in 1970 by Alfano and Shapiro [3]. Supercontinuum generation is the production of ultra-broadband spectrum pumped by a high power laser source- femtosecond pumped pulse, in our case. A photonic crystal that has 1.2 μm core diameter and zero group dispersion at 750 nm was used to produce broadband (450-1150nm) continuum. A characteristic spectrum is shown in Figure 2.

3. Experimental Techniques

CARS microspectroscopy

CARS as spectroscopic technique was first reported in 1965 [4], showing that two coherent light beams of frequency w1 and w2 can be used to drive a Raman vibrational mode at frequency $\omega_R = \omega_1 - \omega_2$. When the two beams are overlapped in space and time, it was observed $\omega + \omega_R$ signal, which is the CARS signal.

Experimental set up

The experimental set up is schematically shown in Figure 3. The two pulses that are needed to coherently drive lattice vibrations within a sample's macroscopic volume are provided by synchronously pumped optical parametric oscillators (OPOs) running at 76 MHz. The OPOs were simultaneously pumped by a split output of a high-power mode-locked Ti:sapphire oscillator tuned to 765 nm. The OPOs with pulsed outputs at 970-1020 nm and 1050-1100 nm, served to coherently drive lattice vibrations, and another small part of the Ti:sapphire oscillator was delayed and served as a probe pulse. All of the three pulses were intrinsically synchronized, made to overlap in space and time, and focused by a high numerical aperture (NA~1.25) objective lens. Actual set up of CARS spectroscopy is also shown in figure 4.

Measurement procedure

The signal detection system is shown in figure 5. We use a high numerical aperture (NA~0.9) (Olympus model: UplanSApo-60x/1.20 W IR) condenser followed by a diffraction grating and a set of bandpass filters. This permitted efficient detection of the signal of interest on the background of other signals generated within the focal

volume. A photomultiplier tube (PMT) with high gain and quantum efficiency (Hamamatsu model #R10699) is used to detect anti-Stokes signal photons at selected wavelengths. The PMT current output is digitized by a high-speed data acquisition card (DAQ, NI-6361). Using this experimental arrangement, we can routinely detect CARS signals versus probe pulse delay times within five decades.

4. SHG microspectroscopy

As illustrated in fig 6, SHG is the nonlinear process where the energy of a short optical pulse of frequency ω propagating through a nonlinear medium is converted to a wave of 2ω, at twice the original frequency. SHG is also known as frequency doubling, which is special case of sum frequency generation (SFG).

Experimental set up

We employ high-repetition rate femtosecond Ti:Sapphire oscillator with central wavelength tuned to 750 nm. The beam was coupled into photonic crystal fiber (PCF) with core diameter of 1.2 μm using 40x objective lens (NA=0.75) to generate spectrally stable continuum that stretches from UV (~450 nm) to IR (~1200 nm) with a total power of about 45 mW (for 100 mW incident beam) [figure 1(b) of manuscript-1]. The continuum was dispersed by a pair of prisms and then part of the spectrum, with fairly smooth envelope in the wavelength range of interest, was selected as a fundamental beam. The beam can be angle scanned to provide scanning area of about 200x200 μm^2 in the image plane of the objective and help to select part of a sample of interest for testing. Samples can also be precisely positioned using micrometer driven translation stage.

Measurement procedure

Spectral shape and power of the incoming fundamental beam is detected before the objective with a help of optical spectrum analyzer (Anritsu: MS 9710C). Second harmonic from the sample is collected through the same objective in the backward direction and filtered out with dichroic mirror (DCM)(Semrock) and shortpass filter (SPF) before entering calibrated grating monochromator (Horiba model: iHR320) with cooled and sensitive CCD detector (Syncerity-356399, Horiba) attached to the exit. The SHG signal is also sent to photomultiplier tube (PMT) to enable sample imaging. The SHG signal beam is effectively de-scanned for the signal detection geometry shown here which helps to focus into the monochromator and use narrow slit in order to achieve higher spectral resolutions. Data acquisition have been performed using data acquisition card, in the case of sample imaging, and the monochromator's USB interface, in the case of spectral measurements, with both controlled by LabView interface software.

5. Making 0 (zero) time delay for CARS experiment

One most important condition for generation of a CARS signal is the spatial and temporal overlap of the three color beams. To ensure the spatial overlap two irises were placed after the dichroic mirror, and then the beams were guided in such way that the beams pass through the center of iris. On the other hand, in order to set up the correct timing between the beams, the optical path lengths of all beams were first measured by the measuring tape. In order to take into account the retardation as the beams pass through any optic, an additional lengths equivalent to the thickness of any

optic along each beam path were added to the length that was measured by the measuring tape. After measuring the optical path lengths, translational stages for the delay lines were adjusted to make the path lengths equal.

To find the zero-delay point , a nonlinear optical crystal , Beta-Barium Borate (BBO), was used to observe the sum frequency generation (SFG) signal generated when the two beams are focused at the crystal that are spatially and temporally overlapped.

First Ti:S laser has been directed through the BBO crystal while being blocked the two OPOs. Then by vertically rotating the crystal we find the SFG signal being color as purple. During this work, we also move the crystal holder back and slight slightly to observe the brightest color or optimize the signal. We do it as a warm-up. It is better to work with two OPOs very first. So at this time we block the TiS and unblock the two OPOs.

Upon rotating the crystal, we find the two spots in a white paper which are essentially second harmonic signals of OPOs at two different crystal positions. Now we set the crystal position in between the two spots where we found the second harmonic signal. Now we move mirror backward and forward, the mirror on the translational stage of an extra-cavity of OPO1, to detect the mixing signal. This means that at this mirror's screw position makes zero time delay for two OPOs. We can test it by blocking any OPO. In other words, if we block one of the OPO, the signal disappears.

Now we block the one OPO and unblock the TiS. Very much the same way, we observe the two spots on the white paper and lens behind the crystal as well. We notice blue color signal for OPO and purple for TiS. Then we set the crystal in between the two spots. After that, we detect the mixing signal by rotating the screw

meter of the corner cube (CC) sitting on a translational stage. Before that, we also position the CC by using translational stage controller.

Now all are in zero time delay. We also unblock the other OPO at this time. We see the two mixing signal on the white paper. If we block one OPO, one of the two spots disappears. On the other hand, if we block another OPO (unblock the one which is now blocked), the other spot disappears. This test confirms the zero time delay of the three colors.

While performing the above procedure, we keep the power of OPO1 as 56 mW and 200 mW for OPO2. That means the combined power after DCM1 was 256 mW. During the observation, all light in the lab room was off.

6. Supercontinuum generation setup

The broad band continuum pulses needed for the SHG set-up are based on the generation of the supercontinuum from a photonic crystal fiber (PCF).

Using the beam splitter and the steering mirror, the Tis:S beam is aligned at the optical table where the translational stage is installed. Then we install the fiber on XYZ stage making the aligned parallel between the polarization of TiS beam and the line markers of the polarization direction of the fiber. We align the beam in such way that the height of the Ti:S beam matches to that of facet of the PCF from optical table, and the height was 93 nm. The half wave plate and Glan Thomson polarizer was installed and the laser power initially set to 50 mW by rotating the half-wave plate and placing a power meter after the polarizer. We were very careful so that powers do not exceed 50 mW while aligning to eschew damaging the fiber.

The stage (466A XYZ fixture, Newport Corp.) is installed in order to focus into the fiber by a 40x microscopic objective lens, maintaining the focusing length of the objective and fiber as well. In order to make sure the right focusing, we reflect the beam from the facet back to nearest starring mirror.

At the very first, however, the focusing objective lens was removed and a white paper was placed about five inches away and the beam position was marked. The focusing objective lens was then replaced and the XYZ stage was adjusted to center the beam to the target. The transmitted beam was observed using an IR viewer on the white paper. The vertical and horizontal axes of the stage were alternately fine-tuned until the central spot was minimized and completely diminished and evenly diffused light was observed. The X- axis of the stage along the optical axis of the fiber was adjusted to focus the beam into the fiber core. The steering mirrors were also adjusted to get the maximum output power.

Once the continuum pulse was observed, the input power was increased to 100 mW. Then output power was optimized by fine tuning of the stage and steering mirror as well. The collimating objective lens (20X, Newport Corp.) was then installed. The lens was then adjusted to collimate and adjust the spot size of the output beam.

It is important to note that the properties of the generated continuum pulse are defined by the amount of the coupled power rather than the coupling frequency. The coupled power is the measured power after the collimating objective and power before the focusing objective. The actual set-up is shown in fig 7.

Figure 1

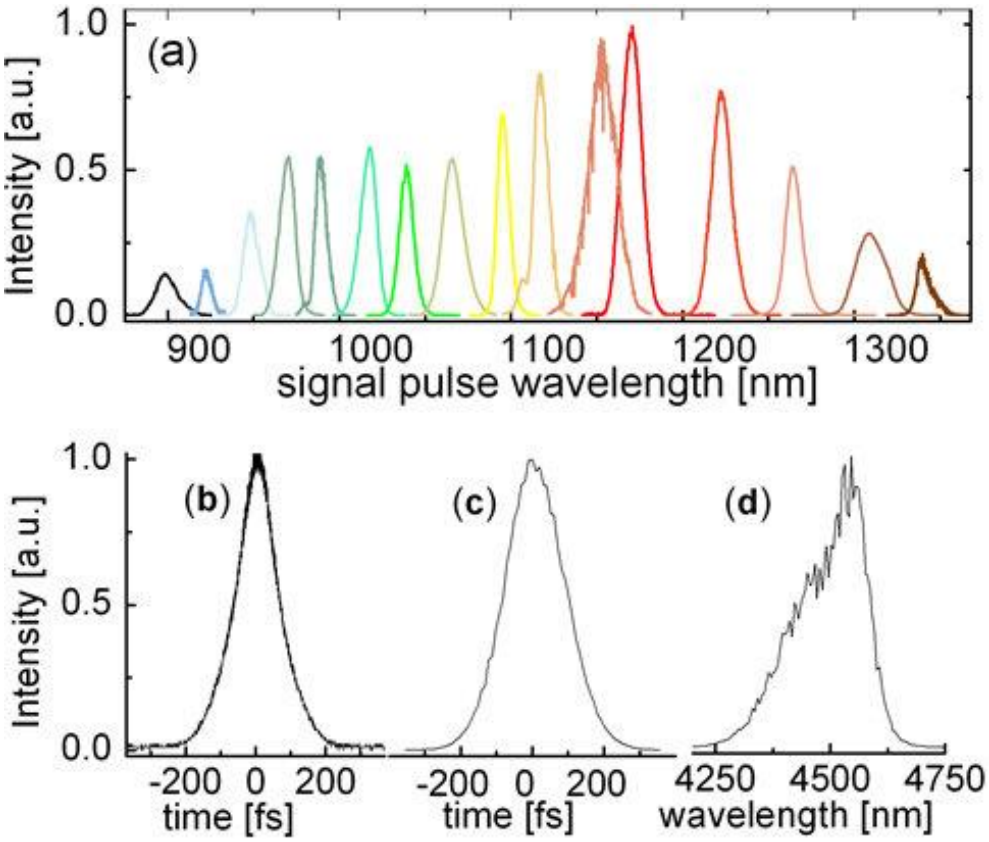

Fig.1. OPO output pulse characteristics (a) shows OPO pulse spectra obtained throughout available tuning range for the OPO. (b),(c) shows typical pulse autocorrelations for signal (b) and idler (c) beams. (d) shows idler pulse spectrum at ~4.5 μm while OPO can still deliver ~50 mW of average power in idler branch.

Figure2

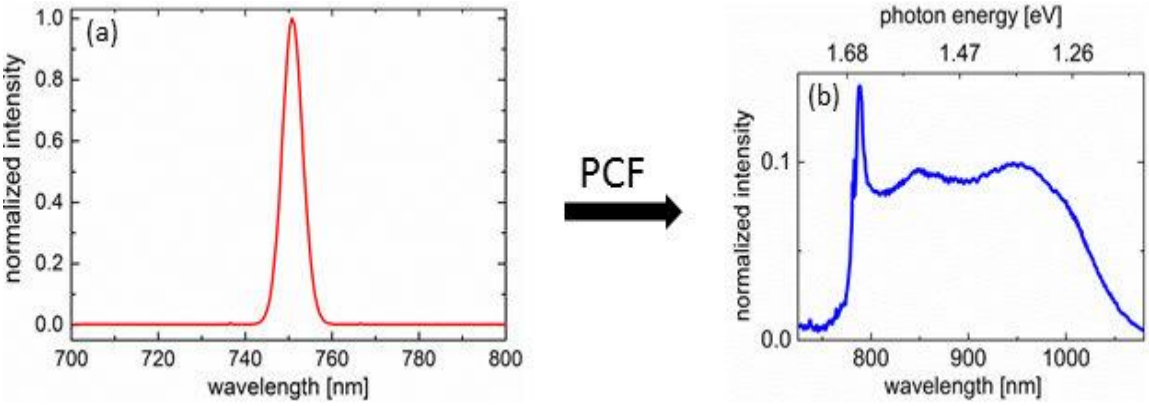

Fig.2. The characteristic curve of a broadband pulse generated by PCF (a) Fundamental pulse of TiS at 750 nm. (b) The output broadband pulse when the 750 nm pulse with energy 150 mW passes through the PCF.

Figure 3

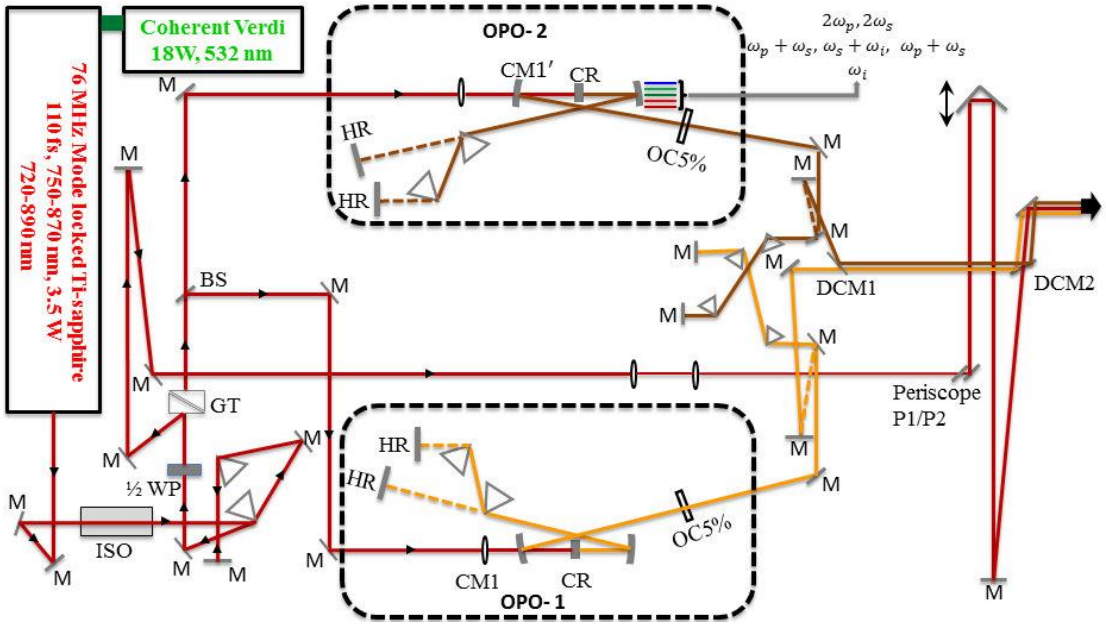

Fig.3. Schematic of the experimental CARS set up. ISO: isolator; WP: wave plate; GT: Glan Thomson polarizer; BS: beam splitter; HR: high reflected mirror; M: mirrors; CR: crystal; OC: output couplers; DCM: dichroic mirrors.

Figure 4

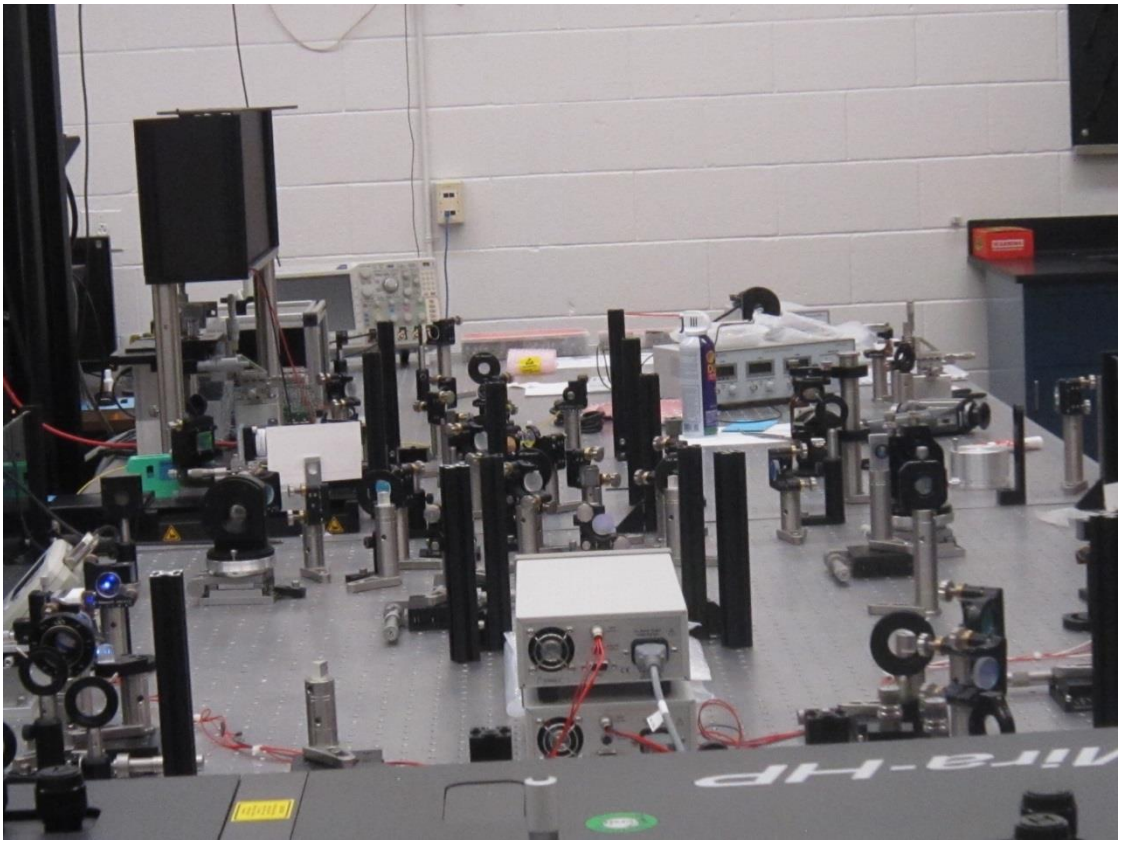

Fig.4. Actual set up of CARS spectroscopy

Figure 5

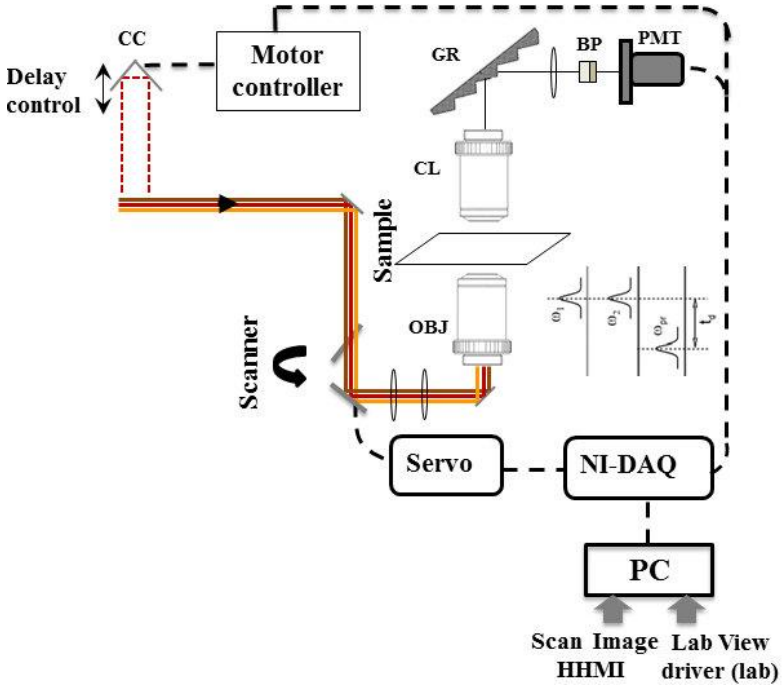

Fig. 5. Schematic diagram of image/data acquisition system. GR: grating; OBJ: objective; CC: corner cube; CL: collimating lens; BP: bandpass filter.

Figure 6

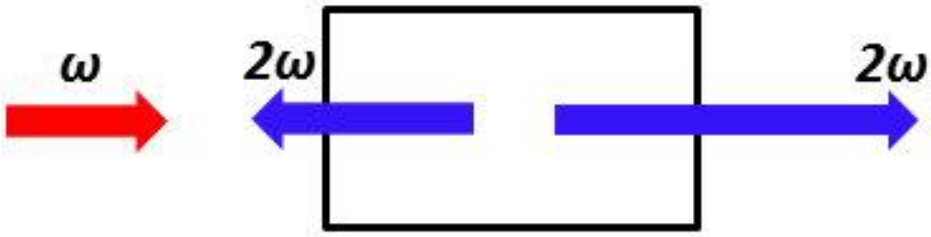

Fig. 6. A schematic diagram of the second harmonic wave of frequency 2ω, generated by a short optical pulse of frequency ω, in the nonlinear medium

Figure 7

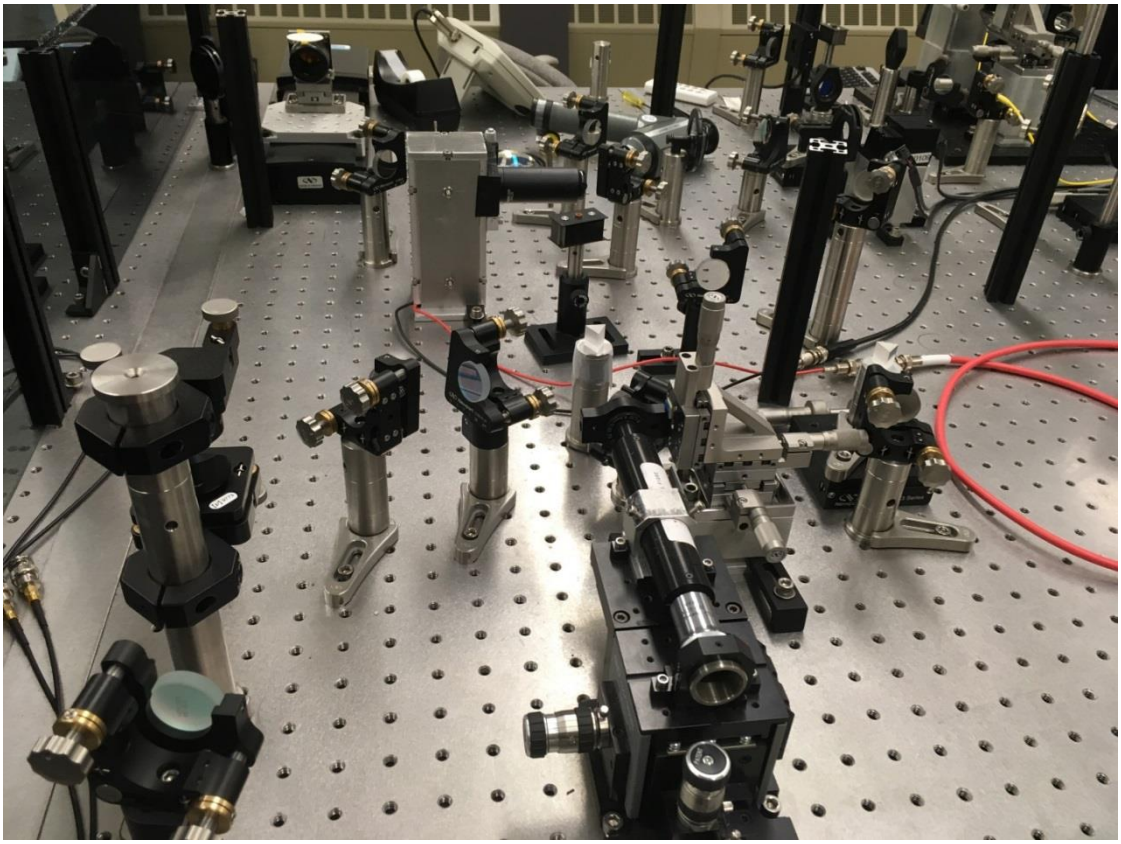

Fig. 7: Actual set up for the continuum generation

MATHMATICAL FORMALISM

SHG intensity solution for undepleted fundamental wave:

In order to derive expression for the second harmonic intensity we start off with the Maxwell's equation. We neglected the free charges and free currents in the equations:

$$\nabla.\vec{D} = 0 \quad (1)$$

$$\nabla \times \vec{E} = -\frac{1}{c}\frac{\partial \vec{B}}{\partial t} \quad (2)$$

$$\nabla.\vec{B} = 0 \quad (3)$$

$$\nabla \times \vec{B} = \frac{1}{c}\frac{\partial \vec{D}}{\partial t} \quad (4)$$

Where $\vec{D}$ is displacement field vector, $\vec{E}$ is the electric field, $\vec{B}$ is the magnetic field, and c is the speed of light. The following relationship between D, E, and P is given by the following equation-

$$D = E + 4\pi P \quad (5)$$

Where P is the incident field induced polarization.

Now solving the two curl equations (2), and (4), and using equation (5), we obtain the following:

$$\nabla \times \nabla \times E + \frac{1}{c^2}\frac{\partial^2 E}{\partial t^2} = -\frac{4\pi}{c^2}\frac{\partial^2 P}{\partial t^2} \quad (6)$$

We can also represent the total polarization (P) as the combination of linear and nonlinear parts ($P= P+P^{NL}$). Using the above two relationships, we can get the following wave equation:

$$-\nabla^2 E + \frac{1}{c^2}\frac{\partial^2 D}{\partial t^2} = -\frac{4\pi}{c^2}\frac{\partial^2 P^{NL}}{\partial t^2} \quad (7)$$

Using the relationship $D=\varepsilon E$, we again obtain

$$-\nabla^2 E + \frac{\varepsilon}{c^2}\frac{\partial^2 E}{\partial t^2} = -\frac{4\pi}{c^2}\frac{\partial^2 P^{NL}}{\partial t^2} \qquad (8)$$

This is the driven wave equation where the right hand part acts as a source term for harmonic signals and P^{NL} represents nonlinear response of the medium due to incident field(s). We will consider this equation to describe the second harmonic generation in a nonlinear optical medium. We consider the electric field and nonlinear polarization field as

$$E_2 = E_2(z)e^{i(k_2 z - \omega_2 t)} + c.c$$

$$P_2 = P_2(z)e^{-i\omega_2 t},$$

$$\text{Where, } P_2 = \chi^{(2)}E_1^2$$

Equation (8) turns into

$$\frac{\partial^2 E_2}{\partial z^2} + 2ik_2\frac{\partial E_2}{\partial z} = -\frac{8\pi\chi^{(2)}\omega_2^2}{c^2}E_1^2 e^{i\Delta k z} \qquad (9)$$

Where Δk represents the phase mismatch between fundamental and harmonic waves while $\Delta k = 2k_1 - k_2$.

Now, we consider slowly varying amplitude approximation which means that the magnitude and the phase of the wave amplitude vary slowly in propagation direction over a length comparable to wavelength. In mathematical from, it can be written as

$$\left|\frac{\partial^2 E_2}{\partial z^2}\right| \ll \left|k_2\frac{\partial E_2}{\partial z}\right|$$

By applying the slowly varying amplitude approximation, the equation (9) becomes

$$\frac{\partial E_2}{\partial z} = \frac{4\pi i\omega_2^2\chi^{(2)}}{k_2 c^2}E_1^2 e^{i\Delta k z} \qquad (10)$$

This is first order differential equation for the second harmonic field. Now the second harmonic field can be obtained by integrating the above equation over the interaction

length L. For the case of undepleted fundamental E_1 is constant over z. Then the final result for the second harmonic field is the following:

$$E_2(L) = \frac{4\pi i\omega_2^2\chi^{(2)}}{k_2c^2}E_1^2\left(\frac{e^{i\Delta kz}-1}{i\Delta k}\right) \quad (11)$$

The intensity of the second harmonic wave is given by the magnitude of the time-averaged Poynting vector,

$$I_2 = \frac{n_2c}{2\pi}|E_2|^2 \quad (12)$$

Using the solution (11) for the field in equation (12) we can obtain

$$I_2 = \frac{8n_2\pi\omega_2^4|\chi^{(2)}|^2}{k_2^2c^3}|E_1^2|^2L^2\left|\frac{sin\left(\frac{\Delta kL}{2}\right)}{\left(\frac{\Delta kL}{2}\right)}\right|^2 \quad (13)$$

Now expressing the incident field in terms of the intensity, we have the second harmonic intensity as

$$I_2 = \frac{128\pi^5}{n_1^2n_2\lambda_2^2c}\left|\chi^{(2)}\right|^2I_1^2L^2sinc^2\left(\frac{\Delta kL}{2}\right) \quad (14)$$

SHG in bulk media under tight focusing condition

Note that the solution (14) is for the power density. I_2 and I_1 are expressed in power densities. Power density is proportional to the square of the electric field, or alternatively the power divided by the beam size. Now the question is if we try to do the experiment, instead of having power density, how much power we have in the second harmonic power in Watts, or energy in Joule.

So the power density does not provide the real solution. If we focus the beam, and we want to know the power in the output power in Watt, we take into account the focusing factors.

The second harmonic power in Watt for this system is given by the following expression:

$$W_2^B = \frac{2\omega_1^2|\chi^{(2)}|^2}{\varepsilon_0 c^3 n_1^2 n_2 \pi}\frac{1}{w_0^2}4l_f^2 W_1^2 \qquad (15)$$

Where, l_f is the effective length of focus and is defined by

$$l_f = \frac{\pi}{2}kw_0^2 \qquad (16)$$

Now we obtain

$$W_2^B = \frac{8\pi\omega_1^2|\chi^{(2)}|^2}{\varepsilon_0 c^3 n_2}\frac{1}{\theta^2}W_1^2 \qquad (17)$$

Where we have introduced the expression:

$$w_0 = \frac{\lambda}{\pi\theta}$$

$$\theta = \frac{\lambda}{\pi w_0}$$

Where, θ is the numerical aperture of the objective, w_0 is the spot size of the beam, and λ is the fundamental wavelength.

Note that equation (17) is derived considering the fact there are no interface. In other words, the crystal is immersed in the medium in such a way that the refractive indices match.

However, in our case, the beam is incident from air to crystal. In order to that feature into account, we consider the following transmission factors:

$$T_{1,2} = \left(\frac{2}{1+n_{1,2}}\right)^2 \qquad (18)$$

Where,n_1 is the refractive index of the fundamental beam in the crystal, and n_2 is the refractive index of the second harmonic in the crystal.

Using the factors of equation (18), the equation (17) becomes

$$W_2^B = \frac{8\pi\omega_1^2|\chi^{(2)}|^2}{\varepsilon_0 c^3 n_2}\frac{1}{\theta^2}\left(\frac{2}{1+n_1}\right)^4\left(\frac{2}{1+n_2}\right)^2 W_1^2 \qquad (19)$$

Neglecting the dispersion in the crystal, i.e., the refractive index at fundamental is close to that of at the second harmonic; the equation (19) turns into

$$W_2^B = \frac{8\pi\omega_1^2|\chi^{(2)}|^2}{\varepsilon_0 c^3 n_2}\frac{1}{\theta^2}\left(\frac{2}{1+n}\right)^6 W_1^2 \qquad (20)$$

This equation is very important for our study because it will be used to obtain the absolute value of the second order nonlinear susceptibility.

SHG in two-dimensional crystal

Since we have very thin material, we need to consider the SHG in thin layer. The nonlinear two- dimensional crystal is placed between the linear bulk media. The crystal is treated as a zero-thickness interface, and the second harmonic signal generate from the boundary.

After writing the right boundary conditions and solving, we obtain the second harmonic filed for s and p polarized light as

$$E_{2x} = \frac{-ik_1\chi^{(2)}}{n_1} sin(3\theta)(1+r_\omega)^2(1+r_{2\omega})E_{1x}^2 \qquad (21)$$

$$E_{2y} = \frac{ik_1\chi^{(2)}}{n_1} cos(3\theta)(1+r_\omega)^2(1+r_{2\omega})E_{1x}^2 \qquad (22)$$

The second harmonic is written as

$$I_2 = \frac{1}{2}\varepsilon_0\left|E_{2x}+E_{2y}\right|^2 \qquad (23)$$

The second harmonic power is defined by

$$W_2^{2D} = \int I_2(x,y)dxdy \qquad (24)$$

The total reflected second harmonic power in terms of the input fundamental power can be written as

$$W_2^{2D} = \frac{2k_1^2\xi^2\left|\chi_{2D}^{(2)}\right|^2}{\pi\varepsilon_0 c w_0^2} W_1^2 \qquad (25)$$

Where, ξ is defined as

$$\xi = |(1 + r_\omega)^2(1 + r_{2\omega})|^2$$

Where, r_ω is reflection coefficient at fundamental and $r_{2\omega}$ is the reflection coefficient at second harmonic.

The equation (25) will also be used for absolute calibration of second order nonlinearity.

To estimate the second order nonlinearity, we normalize the two-dimensional second harmonic data to the one obtained from the reference crystal.

We obtain a ratio from equations (20) and (25) which will essentially provide the dispersion of the absolute value of second order nonlinear susceptibility:

$$\frac{W_2^{2D}}{W_2^B} = \frac{n(n+1)^6\theta^2\left|\chi_{2D}^{(2)}\right|^2\xi^2}{256\pi^2 w_0^2\left|\chi^{(2)}\right|^2} \equiv \rho \qquad (26)$$

Now we can write the expression for the absolute value of second order nonlinearity in terms of the known reference crystal's nonlinearity, refractive index, numerical aperture of the objective lens, and the measure ratio:

$$\left|\chi_{2D}^{(2)}\right| = \sqrt{\rho}\,\frac{16\lambda}{(n+1)^3\sqrt{n}\theta^2}\left|\chi^{(2)}\right| \qquad (27)$$

This equation was used to calibrate the second order nonlinear susceptibility in manuscript-2.

CARS theory

At the beginning, it is important to note that CARS signal is generated due to the third order nonlinear susceptibility while the SHG is due to the second order nonlinear susceptibility which is discussed above.

CARS is used to investigate Raman active resonances and modes. In this process, in general, one deal with three different incident waves at frequencies $\omega_1, \omega_2, \omega_3$. During the CARS process, a new wave at $\omega_4 = \omega_3 + (\omega_2 - \omega_1)$ is generated. This new generated wave is called anti-Stokes wave at optical frequency $\omega_{as} = \omega_4$. However, when the opposite happens, i.e., when $\omega_4 = \omega_3 - (\omega_2 - \omega_1)$, then one deals with Coherent Stokes Raman Scattering (CSRS) . CSRS is almost like CARS except for the fact that Stokes wave is detected which is at a lower optical frequency $\omega_{as} = \omega_4$.

CARS can be described as two photon excitation process followed by a two-photon de-excitation process. Combined together the two constitute a resonantly enhanced four-wave mixing process. In an experiment, a degenerate CARS process is realized at least two laser beams with strong intensity. The first beam at the optical frequency ω_2 is often called pump and the second with frequency is ω_1 called Stokes beam. Both beams are focused onto the sample simultaneously. We not that $\omega_2 > \omega_1$. The incident beam excite the corresponding Raman active transition. The same beam at will also serve, for this particular case, as a third or probe beam with frequency $\omega_3 = \omega_2$. The beam is scattered off the excited vibrations to form a wave with frequency $\omega_4 = \omega_2 - \omega_1 + \omega_1 = 2\omega_1 - \omega_2$ which is anti-Stokes that is $\Omega = \omega_2 - \omega_1$ shifted from ω_2. The new wave is resonantly enhanced since frequency difference $\omega_2 - \omega_2$ is matched to Ω as was just mentioned.

$$\Omega = \omega_2(pump) - \omega_2(Stokes)$$

$$\omega_4(anti - Stokes) = \omega_2(pump) + \omega_3(probe) - \omega_1(stokes)$$

Thus the anti-Stokes wave in the CARS process will follow at frequency

$$\omega_{as} = 2\omega_2 - \omega_1$$

If the ω_2 frequency is tunable a dispersion of the corresponding $\chi^{(3)}$can be measured by detecting anti-Stokes wave's intensity.

The third-order nonlinear polarization is used as a driving force in Maxwell's equations for the anti-Stokes field. In general, a set of coupled wave equations involving pump, Stokes, and anti-Stokes waves should be solved in order to obtain the coherent anti-Stokes field amplitude and the corresponding intensity.

The polarization drives the anti-Stokes field that builds up along the beam's interaction path and can be calculated using the following wave equation that is derived from the Maxwell's equations:

$$\nabla^2 \vec{E}_{as} - \frac{1}{c^2}\frac{\partial^2 \vec{E}_{as}}{\partial t^2} = \mu_0 \frac{\partial^2 P^{(3)}_{CARS}}{\partial t^2} \qquad (28)$$

Where E_{as} is the electric field amplitude at anti-Stokes frequency of $\omega_2 - \omega_1 + \omega_3$. As was mentioned above, the four waves $E_{as}, E_1, E_2, and\ E_3$ (embedded into nonlinear polarization term$P^{(3)}_{CARS}$), should interact in an efficient way so that their phase match along the path. In this case, the interaction yields in strong CARS signal. In order to demonstrate this we will consider a case of degenerate CARS (i.e., $\omega_{as} = \omega_2 - \omega_1 + \omega_2 = 2\omega_2 - \omega_1$) with the three waves propagating along the same z-direction, i.e., a collinear interaction. A solution to the equation () will be sought in the following format:

$$E_{as}(z,t) = E_{as}(z)e^{-i(\omega_{as}t - k_{as}z)} \qquad (29)$$

Also, we will assume that the CARS process efficiency is rather low so that (a) we can apply slowly varying (along z) amplitude approximation approach, and (b) assume that fields $E_1(z)$ and $E_2(z)$ are not attenuated or depleted in the interaction process (i.e., $E_1(z) = E_1 e^{-i(\omega_1 t - k_1 z)}$, $E_2(z) = E_2 e^{-i(\omega_2 t - k_2 z)}$).

Taking into account equation (29) and the two conditions, equation (28) transforms into a simpler, first order differential equation:

$$\frac{\partial E_{as}(z)}{\partial z} = \frac{ik_{as}}{2n_{as}} \chi^{(3)} E_1 E_2^2 e^{-i(2k_2 - k_1 - k_{as})z} \qquad (30)$$

The solution for the anti-Stokes field E_{as} is straightforward for the interaction length L. For the amplitude $E_{as}(L)$ at the medium's output we obtain the following:

$$E_{as}(L) = \frac{ik_{as}}{2n_{as}} \chi^{(3)}_{CARS} E_1 E_2^2 \left(\frac{sin\left(\frac{\Delta kL}{2}\right)}{\left(\frac{\Delta kL}{2}\right)} \right) L \qquad (31)$$

$$\Delta k = 2k_2 - k_1 - k_{as}$$

Further, assuming field-intensity relationship,

$$I_{CARS} = 2cn_{as}\varepsilon_0 (E_{as}(L))^2$$

We finally obtain for CARS signal intensity

$$I_{CARS} = I_{CARS(0)} \left| \frac{sin\left(\frac{\Delta kL}{2}\right)}{\left(\frac{\Delta kL}{2}\right)} \right|^2 \qquad (32)$$

$$where\ I_{CARS(0)} = \frac{k_{as} L^2}{16 n_{as} n_1 n_2^2 \varepsilon_0} \left|\chi^{(3)}\right|^2 I_1 I_2^2$$

Here we used the relationship for intensities and fields $E_1^2 = \frac{I_1}{2cn_1\varepsilon_0}$

MATLAB CODES

Codes for getting SHG signal change across the image used in manuscript-1

```
%loads image data (500x500 pixel^2) saved within the image data
acquisition Labview driver
%'continuos...vi' and plots it in 3D colormap, the image is cropped
at
%pixel positions noted below (see command line 12)
close all
%path='/Volumes/USB
DISK/manuscripts/Optics_Letters/figures_data/figure_2/';
%addpath(path)
%fullname='/Volumes/USB
DISK/manuscripts/Optics_Letters/figures_data/figure_2/wse2_image_data
.dat';
%dlmread(fullname);
importdata('wse2_image_data.txt');
IM1=flipud(ans);
IM2=rot90(IM1,-2);
IM2D=130*(IM2+0.008);
IM3D=IM2D(160:340,140:360);
figure('Position',[400 400 900 540])

%draw horizontal dashed line at vert pixel 100 accross the image
IM3D(100,1:10)=100;IM3D(100,21:30)=100;IM3D(100,41:50)=100;IM3D(100,6
1:70)=100;
IM3D(100,81:90)=100;IM3D(100,101:110)=100;IM3D(100,121:130)=100;IM3D(
100,141:150)=100;
IM3D(100,161:170)=100;IM3D(100,181:190)=100;IM3D(100,201:210)=100;
IM3D(170,190:207)=100;

%plot image in RGB
image(IM3D)
hot(128)
colormap(hot)
axis image
axis off
text(190,164,'5\mum','Color','y','Fontsize',6)

set(gcf, 'PaperPositionMode', 'manual');
set(gcf, 'PaperUnits', 'inches');
set(gcf,'PaperSize',[8.5,11]);
set(gcf, 'PaperPosition', [0.69 6.875 4.4 2.6]);
print -f1 -r600 -dtiff Fig2a

%take crossectional data accross horizontal line at pixel 99 and save
it
line1=IM3D(99,:);
pixel=1:221;
figure (2)
hold on
plot(pixel,line1)
section=[pixel' line1'/20]
```

```
%fullname2='/Volumes/USB
DISK/manuscripts/Optics_Letters/figures_data/figure_2/cross_section_d
ata_pix100Y.dat';
%dlmwrite(fullname2,section,'\t')
```

These codes were used in manuscript-3 to fit the CARS data:

```
%manual parameter fit to experimental CARS signal - simulates CARS
signal (trapezoid integration method is used)
clear variables
close all

%fname1=strcat('/Volumes/VERBATIM/best_KTP_data/for_papers/',...

%'APL_fig_v2/Fig_3/Figure_3a_ktp_cars_967_1051_good_spectrum_01.dat')
%fname1=strcat('D:\best_oil_data\data27\oil_cars_target1280_965_1100_
repeat.dat');
%for windows PC

fname1=strcat('C:\Users\carruba\Documents\MATLAB\CARS_sig_fit\oil_123
9cm-1_968nm_1100nm_1.dat');%for MAC

dlmread(fname1);
time11=ans(:,1)-260;signal11=ans(:,2);
figure (1)
semilogy(time11,signal11,'bo')

c=2.99792e10;                       %speed of light in [cm/s]

l1=965;l2=1100;                     %OPO1 and OPO2 wavelengths in [nm]
w1=1e7*2*pi*c/l1;w2=1e7*2*pi*c/l2;        %OPO1 and OPO2 freq in [Hz]
wt=w1-w2;                                  %target frequency [Hz]
wtcm=wt/(2*pi*c);                         %target frequency in [cm-1]
norm=1e-15;                          %[fs] to [s] translation constant
norm1=6.2e43;


%calculating coeherent amplitude Q(t)
nuR1=1268;wR1=2*pi*nuR1*c;%Raman shift in [cm-1] and in [Hz] for
first peak
nuR2=1317;wR2=2*pi*nuR2*c; %Raman shift in [cm-1] and in [Hz] for
second peak
nuR3=0;wR3=2*pi*nuR3*c;  %Raman shift in [cm-1] and in [Hz] for third
peak

wr1=(wt-wR1)*norm;wr2=(wt-wR2)*norm;      %detunings in [fs-1]
wr3=(wt-wR3)*norm;

tp1=335;tp2=335;                    %pulsewidth of I1 and I2 in [fss]
a12=-2*log(2)*(1/tp1^2+1/tp2^2);    %pulsewidth coeff at the Gaussian
envelope func

T21=550;T22=670;T33=1400000;T44=10;    %dephasing times in [fs]

b21=-1/T21-1i*wr1;
b22=-1/T22-1i*wr2;
b33=-1/T33-1i*wr3;
b44=-1/T44-1i*wr1;
```

```
phi1=0;
A1=0.033;                                          %relative ampl of peak 1
A2=0.129;                                          %realtive ampl of peak 2
A3=0;                                              %.................peak 3
A4=40;                                          %.................NR backgr
floor=3.1e-45;

step0=2;
tmin=-2000;tmax=5000;step1=2;
t1=tmin:step1:tmax;m1=length(t1);
lim=5*tp1;
ts=-lim:step0:lim;
for j1=1:m1
    t=t1(j1);
    if t<-lim
        hs=zeros(1,length(ts));
    elseif t>lim
        hs=ones(1,length(ts));
    else
        p1=round((t+lim)/step0);
        hs=[ones(1,p1) zeros(1,(length(ts)-p1))];
    end
    F1=hs.*(A1*exp(b21*(t-ts)+phi1)+A2*exp(b22*(t-ts))...
        +A3*exp(b33*(t-ts))+A4*exp(b44*(t-ts))).*exp(a12*ts.^2);
%integrand G(t-t')*f(t')
    Q(j1)=step0*trapz(F1);
end
Q11=(norm*abs(Q)).^2;
%figure (1)
%semilogy(t1,Q11,'b-','LineWidth',2)
%set(gca,'FontSize',14)
%axis([-1500 9000 1e-8*max(Q11) 2*max(Q11)])
%xlabel('time delay [fs]','FontSize',14)
%ylabel('abs(Q^2)','FontSize',14)

%convolution of the absolute value...
%squared Q with probe pulse

tp3=100;
a3=-4*log(2)*(1/tp3^2);step2=2; %pulsewidth coeff at the Gaussian
envelope func
td=(tmin+5*tp3):step2:(tmax-5*tp3);m2=length(td);  %time delay

for j2=1:m2
    I3=sqrt(-a3/pi)*exp(a3*(t1-td(j2)).^2);
    F2=Q11.*I3;
    signal(j2)=norm1*(norm*step2*trapz(F2)+floor)-0.9e-1;
end
hold on
semilogy(td,signal,'r-','LineWidth',2)


set(gca,'FontSize',14)
axis([(tmin+5*tp3) (tmax-5*tp3)+1000 8e-6*max(signal11)
2*max(signal11)])
xlabel('time delay [fs]','FontSize',14)
```

```
ylabel('CARS signal [a.u.]','FontSize',14)
D1=[(td+0)' signal'];
%fname2=strcat('D:\best_oil_data\data27\oil_cars_target1280_965_1100_
repeat_best_fit.dat')
fname2=strcat('C:\Users\carruba\Documents\MATLAB\CARS_sig_fit\best_oi
l_data\data23\oil_1239cm-1_968nm_1100nm_1.dat');
%dlmwrite(fname2,D1)
```

SOFTWARE USED IN THIS THESIS

Front view of LabVIEW: SHG spectra

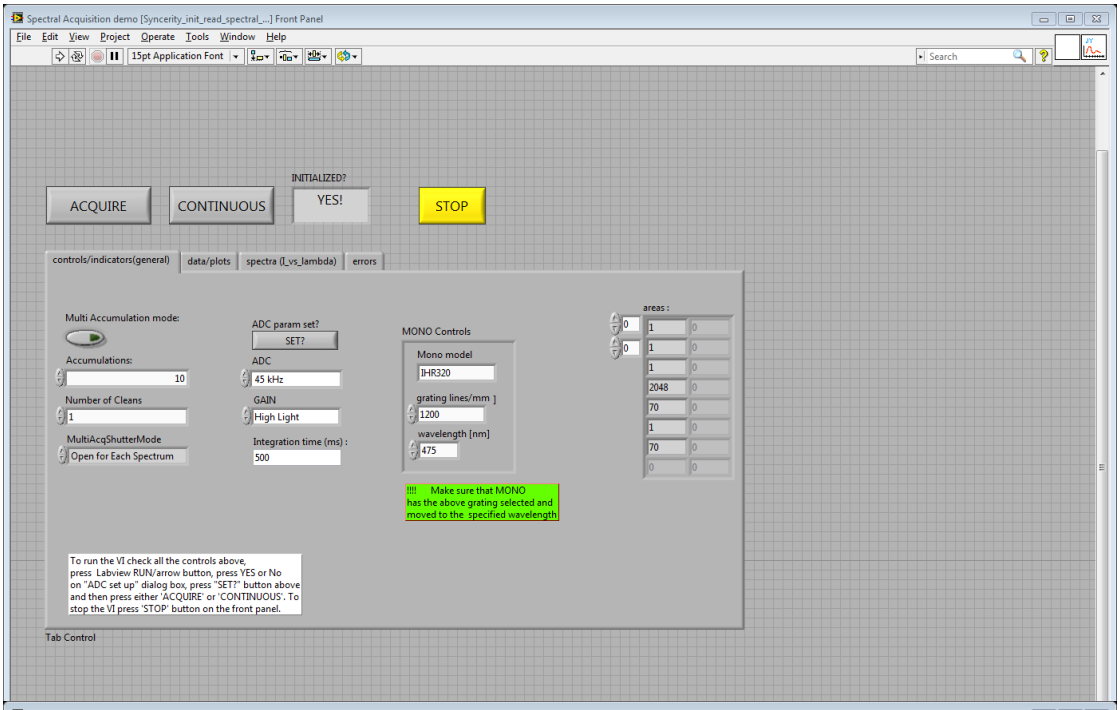

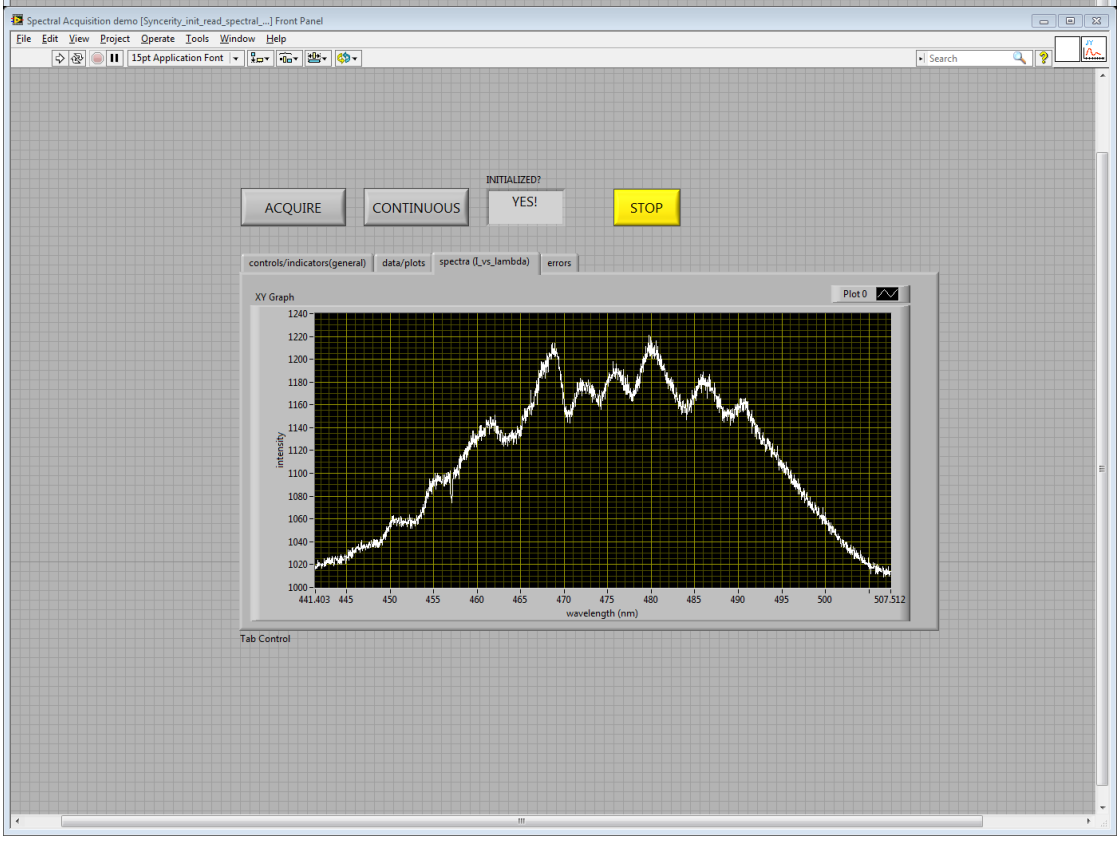

Front view of LabVIEW: SHG image

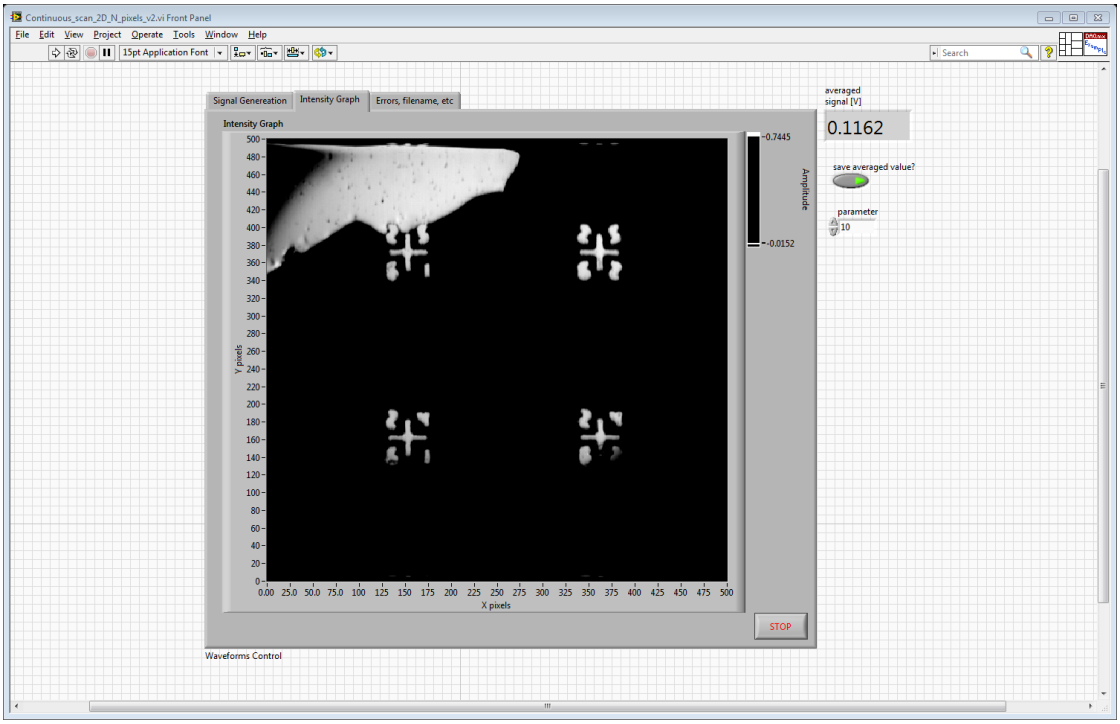

Front view of LabVIEW: CARS spectra

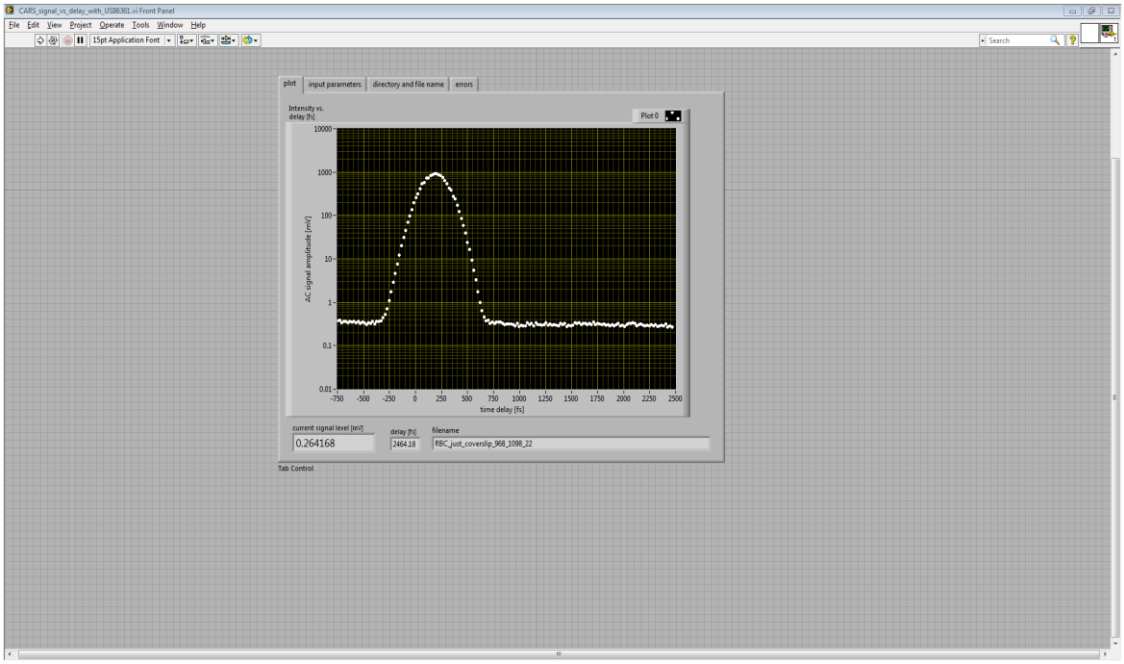

BIBLIOGRAPHY

MANUSCRIPT-1

Bloembergen, N., Pershan, P.S., "Light Waves at the Boundary of Nonlinear Media," *Physical Review*, 128, 1962, 606-622.

Boyd, G.D., and Kleinman, D.A., "Parametric interaction of Focused gaussinan light beams ," *Journal of Applied Physics***, 39,** 1968, 3597-3639.

Dmitriev, V. G., Gurzadyan, G. G., *Handbook of Nonlinear Optical Crystals* (Springer Series in Optical Sciences), 1996, 2d Edition.

Eichfeld, S.M., Eichfeld, C.M., Lin, Y-C., Hossain, L.,and Robinson, J.A., "Rapid, non-destructive evaluation of ultrathin WSe2 using spectroscopic ellipsometry," *APL Materials* ,2, 2014, 092508 .

Kumar, N., Najmaei, S., Cui, Q., Ceballos, F., Ajayan, P. M., Lou, J., and Zhao, H. , "Second harmonic microscopy of monolayer MoS_2," *Physical Review B*, 87,2013, 161403-5.

Li, Y., Rao, Y., Mak, K.F., You, Y., Wang, S., Dean, C.R., and Heinz ,T.F., " Probing symmetry properties of Few-layer MoS_2 and h-BN by optical second-harmonic generation," *Nano Letter*, 13, 2013, 3329-3333 .

Leitsmann, R. , Schmidt, W.G., Hahn, P.H., and Bechstedt, F., "Second-harmonic polarizability including electron-hole attraction from band-structure theory," *Physical Review B*, 71, 2005, 195209 .

Malard, L., M., Alencar, T. V., Barboza, A.P.M., Mak, K. F., and de Paula, A.M., "Observation of intense second harmonic generation from MoS_2 atomic crystals," *Physical Review B*, 87, 2013, 201401-5

Merano, M., "Nonlinear Optical Response of a Two-dimensional atomic crystal," *Optics Letter*, 41, 2016, 187-190

Merano, M., "Fresnel coefficients of a two-dimensional atomic crystal," *Physical Review A*, 93, 2016, 013832

Mishina, E., Sherstyuk, Lavrov, N., Sigov, S., A., Mitioglu,A., Anghel, S., and Kulyuk, L. , "Observation of two polytypes of MoS_2 ultrathin layers studied by second harmonic generation microscopy and photoluminescence," *Applied Physics Letter*, 106, 2015, 31901-5.

Radisavljevic, B., Radenovic, A., Brivio, J., Giacometti, V.,and Kis, A., "Single-layer MoS_2 Transistors," *Nature Nanotechnology*, 6, 2011,147-150

Ramasubramaniam, A., "Large excitonic effects in monolayers of molybdenum and tungsten dichalcogenides," *Physical Review B,* 86, 2012, 115409-6.

Shoji, I. , Kondo, T., Kitamoto, A., Shirane, M. , and Ito, R., "Absolute scale of second-order nonlinear-optical coefficients,"*Journal of the Optical Society of America*, 14, 1997, 2268-2294 .

Supplement

Trolle, M. L., Seifert, G., and Pedersen,T. G., "Theory of excitonic second harmonic generation in monolayer MoS_2," *Physical Review B*, 89, 2014, 235410 .

Vodopyanov, K., Levi, O., Kuo, Pinguet, P. T., Harris, J., Fejer, M., Gerard,

Becouarn, B., L. , and Lallier, E., “Optical parametric oscillation in quasi-phase-matched GaAs” *Optics Letter*, 29, 2004, 1912-1914 .

Wang, G., Marie, X., Gerber, I., Amand, T., Lagarde, D., Bouet, L., Vidal, Balocchi, M., A., and Urbaszek, B., "Giant Enhancement of the Optical Second-Harmonic Emission of WSe_2 Monolayers by Laser Excitation at Exciton Resonances," *Physical Review Letter*, 114, 2015, 097403-6.

MANUSCRIPT-2

Baker, S., Walmsley, I., J., Tisch, W.G., and Marangos, J.P., “Femtosecond to attosecond light pulses from a molecular modulator.” *Nature Photonics*, 5, 2011, 664-671 (2011)

Bhupathiraju, K., Seymour, A., Ganikhanov, F., “*Femtosecond optical parametric oscillator based on periodically poled LiTaO3 crystal.* ” *Optics Letter*, 34, 2009, 2092-20194

Bushiri, M.J., Pillai, V.P. M., Ratheesh, R., and Nayar, V.U., “Raman spectra of KTP crystal in an in situ electric field” *Journal of Physics and Chemistry of Solids*, 60,1999,1983-1988.

Bushiri, M.J., and Nayar, V.U., “Structural aspects of $KMg_{1/3}Nb_{2/3}PO_5$ (KMNP), A KTP analogue — Raman and FTIR spectroscopic study.” *Journal of Nonlinear Optical Physics & Materials*, 10, 2001, 345-353.

Chen Y.F., “Stimulated Raman scattering in a potassium titanyl phosphate crystal: simultaneous self-sum frequency mixing and self-frequency doubling ” *Optics Letter*, 30, 2005, 400-402.

Ferrer, Ch., Segura, A., Andres, M.V., Munoz, V., and Pellicer, "The application of the photoacoustic transmittance oscillations for determining elastic constants in gallium and indium selenides" J., *Journal of Applied Physics*, 79, 1996, 3200-3204.

Fursawa, S., Hayasi, H., Ishibashi, Y., Miyamoto, A., and Sasaki, T., "Raman Scattering Study of $KTiOPO_4$ (KTP) Single Crystal" *Journal of the Physical Society of Japan*, 60, 1991, 2470-2474 .

Garmash, V.M., Govorun, D.N., Korotkov, P.A., Obukhovskii, V.V, Pavlova, N.I., and Rez, I.S ., "Raman spectrum of a $KTiOPO_4$ single crystal" *Optical Spectroscopy*, 58, 1985, 424-426.

Jerry, A., *Introduction to Integral Equations With Applications*, (2d edition, John Willey and Sons, Inc.,1999)

Kourouklis, G.A., Jayaraman, A., and Ballamn, A.A., "A high pressure Raman study of KTP and pressure induced phase transitions " *Solid State Communications*, 62, 1987, 379-382.

Kugel, G. E., Brehatt, F., Wyncket, B., Fontanat, M. D., Marniers, G., Carabatos-Nedelect, C., and Mangin, J., "The vibrational spectrum of a KTiOPO, single crystal studied by Raman and infrared reflectivity spectroscopy." *Journal of Physics C: Solid State Physics*, 21, 1988, 5565-5583.

Laubereau, A., Von der Linde, D., and Kaiser, W., "Direct Measurement of the Vibrational Lifetimes of Molecules in Liquids." *Physics Review Letter*, 28, 1972, 1162-1165.

Laubereau ,A., and Kaiser, W., "Vibrational dynamics of liquids and solids investigated by picosecond light pulses" *Review of Modern Physics*, 50, 1978, 607-665 .

Liwen, X., Dawei, C., and Hongda, N., "Observation of raman scattering and fluorescent spectra of KTiOPO4 (KTP) crystal" *Chinese Physics Letter*, 6, 1989, 225-228

Losev, L.L., Song, J., Xia, J., Strickland, D., and Brukhanov, V., "Multifrequency parametric infrared Raman generation in $KGd(WO_4)_2$ crystal with biharmonic ultrashort-pulse pumping" *Optics Letter*, 27, 2002, 2100-2102.

Massey, G.A., Loehr ,T.M., Willis, L.J., and Johnson, J.C., ""Raman and electrooptic properties of potassium titanate phosphate."*Applied Optics*, 19, 1980, 4136-4137.

Matsubara, E., Sekikawa, T., and Yamashita, M., "Generation of ultrashort optical pulses using multiple coherent anti-Stokes Raman scattering in a crystal at room temperature" *Applied Physics Letter*, 92, 2008, 071104-3.

Malinovskaya, S. A., "Prevention of decoherence by two femtosecond chirped pulse trains**"** *Optics Letter*, 33, 2008, 2245-2247.

Pasiskevicius, V., Fragemann, A., Laurell, F., Butkus, R., Smilgevicius, V.,and Piskarskas, A., "Enhanced stimulated Raman scattering in optical parametric oscillators from periodically poled KTiOPO4" *Applied Physics Letter*, 82, 2003, 325-327.

Pasiskevicius, V., Canalias, C., Laurell, F., "Highly efficient stimulated Raman scattering of picosecond pulses in KTiOPO4." *Applied Physics Letter*, **88**, 2006, 041110-3.

Rowley, J., Yang, S., and Ganikhanov, F., "Power and tuning characteristics of a broadly tunable femtosecond optical parametric oscillator based on periodically poled stoichiometric lithium tantalite." *Journal of Optical Society of America B*, 28, 2011, 1026-1036.

Savatinova, I., Savova, I., Liarokapis, E., Ziling, C.C., Atuchin, V.V., Armenisek, M.N., Passrok, V.M.N. , "A comparative analysis of Rb:KTP and Cs:KTP optical waveguides" *Journal of Physics D: Applied Physics*, 31, 1998, 1667-1672.

Tu, C.S., Guo, A.R., Tao, R., Katiyar, R.S., Guo, R., and Bhalla, A.S., "Temperature dependent Raman scattering in KTiOPO4 and KTiOAsO4 single crystals" *Journal of Applied Physics*, 79, 1996, 3235-3240.

Vivekanandan, K., Setvasekarapandian, S., Kolandaivel, P., Sebastian, M.T., and Suma, S., "Raman and FT-IR spectroscopic characterisation of flux grown $KTiOPO_4$ and $KRbTiOPO_4$ non-linear optical crystals ." Materials Chemistry and Physics, 49, 1997, 204-210.

Voronki, Y.K., Dyahov, V.A., Kudryavtsev, A.B., Osiko, V.V., Sobol, A.A., E.V. ,and Sorokin, "Raman scattering study of phase transformations in KTiOPO " *Soviet Physics-Solid State*, 31,1989, 1736-1740.

Watson, G.H., "Polarized Raman spectra of $ktioaso_4$ and isomorphic nonlinear-optical crystals." Journal of Raman Spectroscopy, 22, 1991, 705-713.

Yang, S., Wysolmerski, R., and Ganikhanov, F., "Three-dimensional nonlinear microspectroscopy and imaging of soft condensed matter" *Optics Letter*, 36, 2011, 3849-3851.

Yang, S., Adhikari, S., Zhang, L., Wysolmerski, R., Spirou, G., and Ganikhanov, F., "Multi-color ultrafast laser platform for nonlinear optical imaging based on independently tunable optical parametric oscillators" *Applied Physics B: Lasers and Optics*, 111, 2013, 617-625.

Yang, S., and Ganikhanov, F., "Dispersion of the resonant nonlinear optical susceptibility obtained with femtosecond time-domain coherent anti-Stokes Raman scattering" *Optics Letter*, 38, 2013, 4754-4757.

Zhi, M., Sokolov, A., "Broadband coherent light generation in a Raman-active crystal driven by two-color femtosecond laser pulses " *Optics Letter*, 32 , 2007, 2251-2253.

MANUSCRIPT-3

Campagnola, P.J., and Leow, L.M., "Second-harmonic imaging microscopy for visualizing biomolecular arrays in cells, tissues and organisms," *Nature Biotechnology*, 21, 2003, 1536-1360 .

Card, A., Mokim, M., and Ganikhanov, F., "Resolving fine spectral features in lattice vibrational modes using femtosecond coherent spectroscopy" *AIP Advances*, 6 , 2016, 025115-7 .

Christian, F.W., Min, W., Saar, B.G., Lu, S., Holtom, G.R., He, C., Tsai, J.C., Kang, J.X., and Xie, X.S., "Label-free biomedical imaging with high sensitivity by stimulated Raman scattering microscopy," *Science*, 322, 2008, 1857–1861.

Denk,W., Strickler, J.H.,and Webb,W.W., "Two-photon laser scanning microscopy," *Science*, 105, 1990, 73-76 .

Dobson, G., "Spectroscopy and Spectrometry of lipids-Part1." *European Journal of Lipid Science and Technology*, 103, 2001, 815-840.

Eberhardt, K., Beleites, C., Marthandan, S., Matthäus, Ch., Diekmann, S., and J., Popp, "Raman and Infrared Spectroscopy Distinguishing Replicative Senescent from Proliferating Primary Human Fibroblast Cells by Detecting Spectral Differences Mainly Due to Biomolecular Alterations." *Analytical Chemistry*, 89, 2017, 2937-2947.

Evans, C.L., Potma, E.O., Puoris'haag, M., Cote, D., Lin, C.P., and Xie, X.S., "Chemical imaging of tissue in vivo with video-rate coherent anti-stokes Raman scattering microscopy," *Proceedings of the National Academy of Sciences of United States of America*, 102, 2005, 16807–16812 .

Korifi, R., Le Dreau, Molinet, Y., J., Artaud, J., and Dupuy, N., "Composition and authentication of virgin olive oil from French PDO regions by chemometric treatment of Raman spectra," *Journal of Raman Spectroscopy*, 42, 2011, 1540–1547 .

Laubereau, A., and Kaiser, W., "Vibrational dynamics of liquids and solids investigated by picosecond light pulses," *Review of Modern Physics*, 50, 1978, 607-665 .

Liu, W., Wangc, H., Du, J., and Jing, C., "Raman microspectroscopy of nucleus and cytoplasm for human colon cancer diagnosis." *Biosensors and Bioelectronics*, 97, 2017, 70-74.

Meksiarun, P., Andriana, B., Matsuyoshi, H., and Sato, H., "Non-invasive Quantitative Analysis of Specific Fat Accumulation in Subcutaneous Adipose Tissues using Raman Spectroscopy," *Science Reports*, 6, 2016, 37068.

Pfeffer , C.P., Olsen, B. R., Ganikhanov, F., and François Légaré, "Multimodal nonlinear optical imaging of collagen arrays," *Journal of Structural Biology*, 164,

2008, 140-145 .

Rowley, J. D., Yang, S., and Ganikhanov, F., "Power and tuning characteristics of a broadly tunable femtosecond optical parametric oscillator based on periodically poled stoichiometric lithium tantalite," *Journal of the Optical Society of America B,* 28, 2011, 1026-1036 .

Tanabe, K., and Hiraishi, J., "Raman linewidth study of molecular interactions in mixtures of hexafluorobenzene with benzene and with mesitylene." *Journal of Raman. Spectroscopy,* 12, 1982, 274-277.

Thomas, G.J., "Raman spectroscopy of protein and nucleic acid assembles." *Annual review of Biophysics and Biomolecular Structures,* 28, 1999, 1-27.

Volkmer, A., Book, L., and Xie, S.X., "Time-resolved coherent anti-Stokes Raman scattering microscopy: Imaging based on Raman free induction decay " *Applied Physics Letter* ,80,2002, 1505-1507.

Zimmerley, M., Mahou, P., De´barre, Schanne-Klein, D., M., and Beaurepaire, E., "Probing Ordered Lipid Assemblies with Polarized Third-Harmonic-Generation Microscopy," *Physical Review X,* 3, 2013, 011002 .

APPENDIX

Bhupathiraju, K., Seymour, A., and Ganikhanov,F., "Femtosecond optical parametric oscillator based on periodically poled $LiTaO_3$ crystal," *Optics Letter*, 34, 2009, 2092-2094.

Janisch, C., Wang, Y., Wang, Ma, D., Mehta , N., Elı´as, A. L., N.Perea-Lo´pez, Terrones., Crespi, M. V., and Liu, Z., "Extraordinary Second Harmonic generation in Tungsten Disulfide Monolayers" *Scientific Reports*, 4, 2014, 5530 -5.

Marker, P.D., and erhune,R.W., T “Study of optical effects due to an induced polarization third order in electric field strength,” *Physical Review*, 137, 1965, 801-818 (1965)

Rowley, J., Yang S., and Ganikhanov ,F., “Power and tuning characteristics of a broadly tunable femtosecond optical parametric oscillator based on periodically poled stoichiometric lithium tantalate,” *Journal of Optical Society of America B*, 28, 2011, 1026-1036.